# Space for Shore

**ESA EOEP-5**

**Coastal Erosion**

# *Technical Specification 3 .0*

| Document history | | | |
|---|---|---|---|
| Version | Authors, Organization | Date | Note |
| 1.0 | Kerstin Stelzer, Brockmann Consult; Arthur Robinet, Virginie Lafon, Olivier Regniers, Benoit Beguet, Aurélie Dehouck, i-Sea; Paulo Baptista, Sandra Fernández, University of Aveiro; Georgia Kalousi, Terra Spatium; Ionut Serban, Terra Signa; Imanol Echave, Harris; Martin Gade, University of Hamburg; Konstantina Bantouvaki, Issaak Parcharidis, Harokopio University of Athens | 12/07/2019 | Version 1.0 Technical Specification |
| 1.1 | Arthur Robinet, i-Sea<br>Georgia Kalousi, Terra Spatium | 13/08/2019 | Improvements following ESA feedback<br>new section for Alignment with EUGENIUS platform |
| 2.0 | Virginie Lafon, i-Sea | 30/09/2019 | Last Improvements following ESA feedback (RIDs detailed in SpaceForShore_TechnicalSpecification-v1.1_ESA) |
| 3.0 | Konstantina Bantouvaki, Issaak Parcharidis, Harokopio University of Athens, Kerstin Stelzer, Prosper Evadzi, Grit Kirches, Brockmann Consult; Silvere Lamy, Virginie Lafon, Olivier Regniers, Nicolas Debonnaire, Manon Besset, i-Sea; Paulo Baptista, Sandra Fernández, University of Aveiro; Georgia Kalousi, Terra Spatium; Ionut Serban, Georgiana Anghelin, Sorin Constantin, Terra Signa; Imanol Echave, Harris; Martin Gade, University of Hamburg; | 20/07/2020 | Version 3.0 Technical Specification: modified algorithm from phase 2 and new algorithm from phase 2 |

# Table of Contents

# 1. SCOPE OF THE DOCUMENT

This document provides an overview of the algorithms proposed by the Space for Shore consortium to produce the main coastal erosion indicators requested by the interviewed end-users (refer to the Requirement Baseline and User Requirement Document Book), which usually address short-time scale monitoring. Some of these algorithms are also designed to produce the latter indicators over longer timescales with the perspective of demonstrating the potential of ESA Earth Observation data archives and other past/currently-growing freely available archives in the study of coastal erosion in the past 25 years at European scale.

The individual algorithms are provided and described by the partners and form the algorithm candidates for the different indicators. A maturity status of the algorithms is given. The document provides further a mapping of algorithms to end-user requirements. Along with these analysis, proposals of algorithms to be used for the different products and pilot sites are then made. The document has been updated with results during the POC, in particular the sections describing the accuracy and maturity of the algorithm as well as the discussions on the relevance of the algorithms to the end-user requirements.

The current version of the Technical Specification Document highlights all algorithms used during the second phase of the project (Table 2-2). In the annex, we present a list of algorithms that were used in phase one and are not exploited anymore (5. Annex).

# 2. INTRODUCTION

Based on the end-user requirements, a grouping of coastal erosion indicators and their level of priority were provided in the Requirement Baseline document. Overall, 22 end-users had been interviewed within the public sector including national governmental agencies, regional authorities, intermunicipal cooperation and municipalities, as well as natural site managers, research centers and coastal observatories. From this panel of potential users of Space for Shore services, more than 40 products were requested to support current and future practices to manage issues related to coastal erosion. To help synthetize end-user requirements these products were grouped in 5 product families. This task enabled to fully characterize the end-user needs in terms of product accuracy as well as the update and delivery frequency. It also evidenced that some products were systematically requested by end-users of different regions of interest, while others were mentioned only by one or two end-users.

The algorithms that are described in this Technical Specification document are organized in five algorithm groups. These groups were built to ease the presentation of the algorithms, as many of these aim at producing similar outputs and/or apply with similar environmental constrains. Each algorithm group is introduced by an introductory and a state-of-the-art section followed by the description of the main features of algorithms (input data, algorithm type / processing chain, output products and tools needed). In addition, information about validation and application range is given for each algorithm. This also includes the information on whether an algorithm is mature enough or shall be tested. All these descriptions are provided in Chapter 3.

*Table 2-1 - Summary of the main products requested (denoted by yellow colour cells) by interviewed end-users to monitor erosion along European coasts, which covers a wide range of geomorphological and environmental conditions. Extracted and adapted from the Requirement Baseline.*

| Family name | Product name | Regions of interest | | | | | | | | |
|---|---|---|---|---|---|---|---|---|---|---|
| | | FR AQ | FR NOR | FR PACA | GER WS | GER BS | PT NWC | GR EMT | GR PEL | RO |
| Shoreline | Cliff foot | | | | | | | | | |
| | Cliff apex | | | | | | | | | |
| | Dune foot | | | | | | | | | |

| | | | | | | | | | | |
|---|---|---|---|---|---|---|---|---|---|---|
| Coastal morphological patterns | Waterline (sea/land interface) | | | | | | | | | |
| | Middle of swash zone | | | | | | | | | |
| | Maximum swash (or run-up) excursion during major storms | | | | | | | | | |
| | Sandbar location | | | | | | | | | |
| | Beach width | | | | | | | | | |
| | Tidal creeks: number, length, form, form and number of tidal creek endings | | | | | | | | | |
| | Erosion at tidal creek edges | | | | | | | | | |
| Coastal DEM | Bathymetry | | | | | | | | | |
| Seabed, foreshore and land cover mapping | Underwater seabed type (sandy/rocky/vegetated) | | | | | | | | | |
| | Intertidal / foreshore type (sandy/rocky/shingle/…) | | | | | | | | | |
| | Coastal habitat and land cover mapping (several levels) | | | | | | | | | |

*Table 2-2 - Overview of algorithm groups and algorithms, their maturity level and responsible partner. The last column indicates for which indicators the respective algorithm is relevant.*

| Algorithm Group | Algorithm | Maturity level[1] | Partner | Suitable for: Product Name |
|---|---|---|---|---|
| **DEMS** | **Algorithm 1a**<br>DSM generation from optical data | 3 | i-Sea<br>Terra Spatium | Cliff foot<br>Cliff apex |
| | **Algorithm 1b**<br>DEM generation from SAR data | 3 | Harris | Cliff foot<br>Cliff apex |
| **Water Line and Creek Edge Detection** | **Algorithm 2a**<br>Water line detection using different methods | 2 | I-Sea<br>Brockmann Consult<br>Terra Spatium<br>Terra Signa | Waterline (sea/land interface)<br>Upper swash limit<br>Beach width |
| | **Algorithm 2e**<br>Edge detection tidal creeks using SAR | 1-2 | University of Hamburg | Tidal creeks: number, length, form, form and number of tidal creek endings<br>Erosion at tidal creek edges |
| | **Algorithm 2f**<br>Upper swash limit | 3 | I-Sea | Upper swash limit |
| | **Algorithm 2g**<br>Water line detection using | 1 | Harokopio University | Waterline (sea/land interface) |

| | | | | |
|---|---|---|---|---|
| | binary products from SAR amplitude data | | | |
| | **Algorithm 2j** Decision tree classification based on band ratios and LSU | 3 | Brockmann Consult | From the classification, the position of tidal creeks is determined. Based on a time series of images, the shifting of tidal creeks can be visualized and thus<br>erosion at tidal creek edges is detected<br>Intertidal habitat mapping |
| | **Algorithm 2k** In-land vegetation boundary method based on NDVI index | 1-2 | Terra Spatium | In land vegetation boundary |
| **Extraction of subaerial morphological structures and changes** | **Algorithm 3c** Cliff line extraction using the cross-shore variation of the beach/cliff slope from DEM | 2 | I-Sea | Cliff foot<br>Cliff apex |
| | **Algorithm 3d** Semi-automated linear feature extraction from DEMs | 1 | Terra Spatium | Cliff foot<br>Cliff apex |
| | **Algorithm 3e** Beach width computation | 3 | I-Sea | Beach width |
| | **Algorithm 3h**<br>Dune foot extraction using supervised classification | 2 | I-sea | Dune foot |
| | **Algorithm 3i**<br>Cliff line extraction using supervised classification | 1 | I-sea | Cliff foot<br>Cliff apex |
| | **Algorithm 3j** Top of the cliff movement using PS with ERS and ENVISAT data | 2 | Harokopio University of Athens | Cliff Movement |
| **Bathymetry** | **Algorithm 4b** Quasi-analytical model to retrieve bathymetry from | 3 | I-Sea | Bathymetry |

| | | | | |
|---|---|---|---|---|
| | HR/VHR optical data | | | |
| | **Algorithm 4c** Bathymetry swell inversion (i-Fourier Fast Transform) | 2 | University of Aveiro | Bathymetry |
| | **Algorithm 4c** Bathymetry swell inversion (ii-Wavelet Transform) | 1 | University of Aveiro | Bathymetry |
| **Extraction of submerged morphological structures and changes** | **Algorithm 6a** Submerged sand banks | 3 | Terra Signa<br>I-Sea | Sandbar location<br>Submerged sandbar migration |
| | **Algorithm 6b** Mapping change of sandbars | 1 | Brockmann Consult | Submerged Sandbar / sand ridge location and changes |

[1] Maturity levels:

1 = innovative or experimental algorithm (not tested yet, want to test ideas in POC sties)

2 = Demonstration algorithm: tested on selected test sites in selected images

3 = mature algorithm – well tested, applied and published algorithm

# 3. DETAILED ALGORITHM DESCRIPTION

## 3.1 ALGORITHM GROUP 1: GENERATION OF DEMS

### 3.1.1 Introduction

Digital Elevation Models (DEMs) are used as input for several coastal erosion products, either directly by exploiting the provided 3D information or indirectly though the production of other DEM-derived datasets, i.e. calculation of volumes and 3D lines extraction.

In particular, many different techniques have been developed the past decades for DEM generation, starting from conventional ground topographic surveys (e.g. GNSS techniques), to robust photogrammetric methods and sophisticated computer vision techniques (e.g. structure-from-motion, etc.); that exploit data acquired from several different instruments and sensors. This chapter is focusing on the description of present state-of-the-art DEM generation algorithms applied on satellite, optical and SAR, high (HR) and very high-resolution (VHR) imagery.

### 3.1.2 State-of-the-art

Optical Imagery

In the case of optical satellite data -both for HR and VHR-, the existing state-of-the-art algorithms are covering the hereunder processing steps:

1. Image Pre-processing: In order to improve the radiometric quality and optimize the images for subsequent processing steps, a series of filters are usually applied on the datasets. The most common pre-processing processes encompass noise reduction, contrast and edge enhancement. Noise reduction filters aim at reducing noise, while sharpening edges and preserving corners and one pixel-wide lines (Baltsavias *et al.,* 2001).
2. Image Orientation: In order to achieve the image orientation, a bundle adjustment with the supplied Rational Polynomial Coefficients (RPCs) model is usually deployed. RPCs provide a compact representation of a ground-to-image geometry, allowing photogrammetric processing without requiring a physical camera model. A set of images (with stereo or tri-stereo overlapping) is given to determine the set of polynomial coefficients in the RPCs model to minimize the error. Therefore, RPCs model is a generalized sensor model, which can achieve high approximation accuracy, while Least Square Method (LSM) is usually used to determine the optimal parameter solution of the rational function model. Indeed, the use of Ground Control Points (GCPs) during this computation is providing the best possible accuracy which according to literature review could be sub-pixel (Eisenbeiss *et al*., 2004).
3. DEM Generation Method: Several different matching algorithms are used for DEM generation, starting from the early ones like correlation-based methods (i.e. 2D correlation, 3D correlation) to most advanced ones', like i.e. 3D Least Square Matching, Global and Semi-Global Matching, to more sophisticated computer vision-based algorithms, like Feature Based Matching, Structure-from-motion. In most methods the pyramid image matching scheme is used. In general, a pyramid image matching method stores matching results in low resolution matching and uses these results as initial points for higher resolution matching.

As stated previously, it is both possible to use pairs of satellite images (i) acquired simultaneously along the satellite path ("mono-date" the satellite looking first frontward and then backward) or (ii) at several consecutive dates ("multi-date"). The later has been recently tested on Norman coastal cliffs using a dataset of Pleiades satellite images (Letortu *et al.,* 2020). Several aspects of viewing geometry (incidence angle) in relation with coastal geomorphology (e.g. height and slope of coastal cliffs, shoreline orientation) have to be considered preliminarily. For instance, DEM generation using mono-date stereo images over very high and abrupt coastal cliffs (like in Normandy) appeared not to be appropriate, i.e. when the satellite is looking backward, only the top and plateau of the cliff being imaged, not the cliff face nor the cliff foot. In addition, sun position at the time of image acquisition associated with shoreline orientation may also be considered, due to shadow effects that may occur on cliff face and cliff foot. The same effect can be seen in sand beach areas (Almeida *et al*., 2019), where a DEM generated from a Pleiades stereo product can achieve very high vertical accuracy (under 0.5m) but this accuracy decreases in dune faces where shadows are produced.

SAR Imagery Algorithms

To generate DEM data from a couple of SAR images two choices are available: (i) interferometry and (ii) radargrammetry.

Stereoscopy for SAR data is known as radargrammetry. This technique is similar to optical/photogrammetry, but it uses a couple of SAR amplitude images to match homologous points and produce height (Capaldo *et al.,* 2014). Radargrammetry produces DEMs with a vertical accuracy of a few meters (worse than interferometry) but is very robust to atmospherical conditions.

Interferometry is a technique that benefits from SAR phase information. In a pair of SAR images, the same object generates a signal with a change in phase that is related to a shift in the distance viewer-object. With the appropriate processing this change can be mapped to a height (Small *et al.,* 1996). This technique has been already used in coastal areas (Hong *et al.,* 2006) (Choi et al., 2007), achieving a vertical accuracy close to 1 meter. Anyway, it is a very sensitive technique that could be affected by different factors as atmosphere conditions, loss of coherence (due to changes on surface conditions).

Interferometry is a technique that cannot be used always. Phase information is very sensitive to changes, and variations in a surface can completely destroy phase coherence making DEM extraction impossible. This is the case in vegetation areas, where coherence falls due to continuous “growing” of the observed object. In these cases, a combination of interferometry and radargrammetry can be used. This approach has been already tested on coastal areas (Yu, 2011) (Nikolakopoulos *et al.,* 2015).

Simultaneous data acquisition using a pair of satellites flying closely in formation is the challenge unravelled by DLR with the twin SAR interferometry TerraSAR-X / TanDEM-X mission. The mission provides digital elevation data at 12-m full resolution and with an absolute vertical accuracy of 1 m. Airbus DS and CSTARS has recently launched the commercial “WorldDEM Ocean Shoreline” product based on TanDEM-X which is supposed to provide an up-to-date reference for coastal issues at global scale (applications in glaciology, see Milillo *et al.,* 2019 ).

## 3.1.3 Algorithm 1a - DEM generation from optical data

### 3.1.3.1 Algorithm description

- *Input data*

According to the software used, different sets of optical satellite images can be used for DEM production, including:

- VHR (or HR) optical imagery acquired in stereo or tri-stereo mod, e.g. Pleiades (or SPOT5)
- pair of non-georeferenced VHR (or HR) optical images acquired at subsequent dates with a temporal spacing relatively small with respect to the characteristic temporal scales of the coastal change studied.

Ground Control Points.

- *Algorithms*

We propose two algorithms for DEM extraction from optical data.

1. The first one is the algorithm proposed by Li and Gruen *(Li Z., Gruen A., 2004)*. This algorithm performs these steps:
    - Image pre-processing: edge-preserving filtering and Wallis filtering are applied to images in order to reduce radiometric artefacts (very dark and bright areas) and enhance texture patterns in regular areas.
    - A pyramid of images is generated reducing image scale at each level, then starting from lowest resolution we apply these steps at each level in a cascade:
        - Feature point matching: feature points generated using Foerstner interest operator and matching done by a geometrically constrained cross-correlation method *(Gruen, Zhang, 2003)*. Edge-matching: edges generated by the Canny operator are matched using a shape matching method.

    - Grid point matching: a regular grid of points is matched using a global image matching method with a relaxation technique *(Gruen, Zhang, 2003)*.
  - A final refined matching based on the modified MPGC *(Gruen, 1985)* is performed in order to achieve accuracy in the subpixel range.
2. The second algorithm, performs the following steps:
  - Image Orientation: A bundle adjustment with RPCs model and with the use of GCPs during this computation is be performed.
  - DEM generation method: It is based in the use of two families of matching methods:
    - Feature Based Matching (FMB): FBM is a matching strategy that is very robust. It only needs coarse approximations and is very fast. It has an accuracy of about 1/3 of a pixel. The matching process computes interest values in two images of a matching pair that describe the appearances of features. The matching process determines common features in the pair by means of the computed interest values.
    - Least Squares Matching (LSM): LSM is a matching strategy that is very accurate, but better approximations are required, and it is considered rather slow in comparison to FBM. It is mostly used to refine points obtained from FBM. The accuracy is about 1/10 pixel. The matching process uses a mask created from one image and a template from the second image at a previously matched point. The mask is shifted on the template until the sum of squares of the gradients is minimized.

- *Tools*

ENVI + OPTICALscape (implementing first algorithm)

ArcGIS-ESRI, QGIS, DTMaster stereo, INPHO Photogrammetric Suite by Trimble (implementing second algorithm)

- *Output product*
  - Raster file output: "*.geotiff"

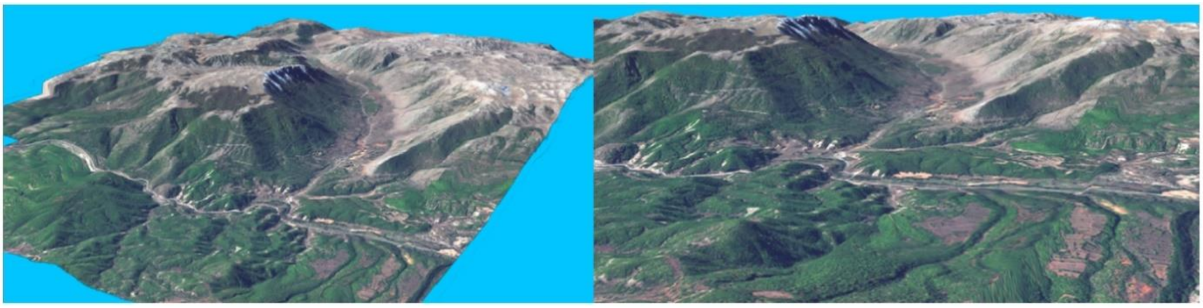

*Figure 3-3 - DEM produced from Very High-Resolution optical stereo satellite imagery (Pleiades, Terra Spatium, ©2016)*

- Vector file output: Point cloud file "*.las"

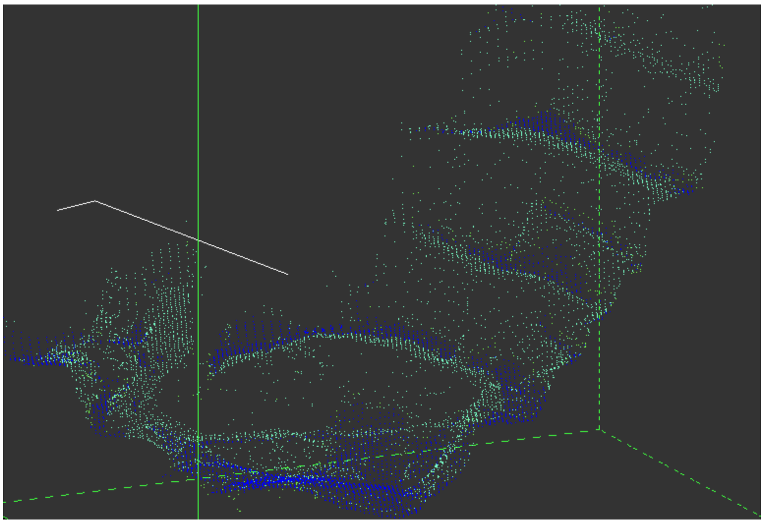

*Figure 3-4 - DEM - Point cloud produced from Very High-Resolution optical stereo satellite imagery over cliff area (Pleiades, Terra Spatium, ©2016).*

### 3.1.3.2 Validation

The deployed algorithms have several times been validated during commercial and research projects executed by Terra Spatium, for areas all over Greece. The algorithms have been tested both in coastal, as well as in-land and mountainous areas, covering all types of morphologies. In these projects, VHR optical satellite data were used to produce DEMs, in particular stereo Pleiades and Geoeye-1 imagery, while computations were performed with the use of Ground Control Points (GCPs). GCPs were collected during *in situ* GPS survey (Real Time Kinematic, L1/L2 frequencies) with a mean horizontal accuracy 2-3 cm. On the same time a set of independent points were collected the so-called Check Points (CPs) and used for validation of the produced DEMs. Usually a set of CPs, evenly distributed along the AOI were chosen, trying to cover the specificities of each region, for every stereo-pair at least 7-8 CPs were collected. At the end of the day, a relative horizontal accuracy of 1 meter and a relative vertical accuracy of 2-3 meters, was achieved in most cases.

In the framework of Space for Shore, a validation campaign will be carried out to assess DEMs production in Greece based on *in situ* GPS measurements. This field work will take place in late-September 2019, mid-October and could be combined along with the validation activities for 4.2.6.2 (Algorithm 2d – Water Line Detection using binary products from SAR amplitude data).

Reference projects:

1. BEACHTOUR National R&D project: A synergy for the sustainable development and safety of the Hellenic Tourist Beaches for the identification of 'best practices' in science-driven beach monitoring, management and decision-making. (2013-2016).
2. ACRITAS National R&D project, Space Technologies for Surveillance and Monitoring of Integrated Applications: research, design, develop and validate integrated space-based surveillance and monitoring applications through advanced multi-sensor data fusion technologies. (2013-2016)
3. Commercial project (National Cadastre & Mapping Agency) Production of VHR ortho-photomaps and DEM along the coastline of Greece. (2007-2009)

### 3.1.3.3 Application range and Maturity

The maturity of the deployed algorithms is considered high, while in order to achieve a high accuracy, Ground Control Points (GCPs) are needed for the computation of the aerial triangulation. The GCPs could be acquired, either directly, through in situ GPS measurements (L1/L2) or indirectly, extracted from pre-existing orthophoto maps of a similar accuracy. Of course, when direct GCPs measurements are being used a better accuracy is achieved at the end of the day, i.e. with measurements deriving from a robust computation with GPS equipment using L1/L2 frequencies. In cases that VHR satellite optical imagery (e.g. Pleiades) is used along with GCPs (measured on the ground) the relative vertical accuracy achieved is around 2-3 meters.

### 3.1.4 Algorithm 1b - DEM Generation from SAR data

#### 3.1.4.1 Algorithm Description

Coastal areas are difficult sites to extract DEM information from SAR data, as they are characterised by low SAR coherence due mainly to the presence of dynamic water bodies and vegetation. This makes unusable the classical interferometry approach, which uses a couple of SAR products to produce an interferogram that contains the changes of phase between both acquisitions. The phase changes are then mapped to elevation variations.

In our case we will use a Multitemporal DINSAR (Differential Interferometry SAR) approach, specifically the SBAS (Small Baseline Subset) technique *(Berardino, Fornaro, Lanari, Sansosti, 2002)* which is well suited for these low SAR coherence areas. This technique makes use of a set of SAR products taken at different times to generate a set of interferograms. The map of these phase changes to terrain displacements creates a set of equations that is inversed by using an SVD decomposition. The aim of SBAS is to find terrain displacements, but it generates also a map of terrain elevation (obtained from the reference DEM used in the process and the residual topographic phase estimated).

The steps performed by SBAS are:

- **Co-registration:** In order to perform calculations between SAR images, a previous co-registration must be done to have all images in the same geometry *(Meijering, Unser, 2004)*. Shift between images is first estimated using sensor position and orientation metadata, then a cross-correlation approach is used for fine-shifting.
- **Interferogram generation:** Once co-registered, SLC (Single-Look Complex) data are used to compute an interferogram, which is obtained by multiplying the one complex image by the conjugate of the other one. The interferogram provides an image of phase changes that are due to different effects *(Monti Guarnieri, Guccione, Pasquali, Desnos, 2003)*.
- **Interferogram flattening:** Interferogram is “flattened” to remove the constant phase effect produced by acquisition geometry and the topographic phase effect produced by terrain slope. In order to flatten the interferogram, a low-resolution DEM (as SRTM) is used to estimate terrain slope.
- **Adaptive filtering:** Once flattened, an adaptive filtering is applied to reduce noise and coherence image is generated *(Baran, Stewart, Kampes, Perski, Lilly, 2003)*. Coherence is a parameter that measures correlation between acquisitions. Only areas with a high coherence value can be used in DEM computation.
- **Phase Unwrapping:** At that point the phase information, which is cyclical, should be unwrapped to provide a linear change. This unwrapping is done using a minimum cost flow method *(Reigber, Moreira, 1997)*.
- **Re-flattening:** This step is performed using ground control points to estimate and remove phase component due to residual topography.
- **Inversion:** SVD inversion is applied to get an estimation of terrain displacements and terrain elevation.
- **Inversion post-processing:** atmospheric effects are filtered from products.
- **Geocoding:** products are transformed from SAR geometry to a cartographic projection.

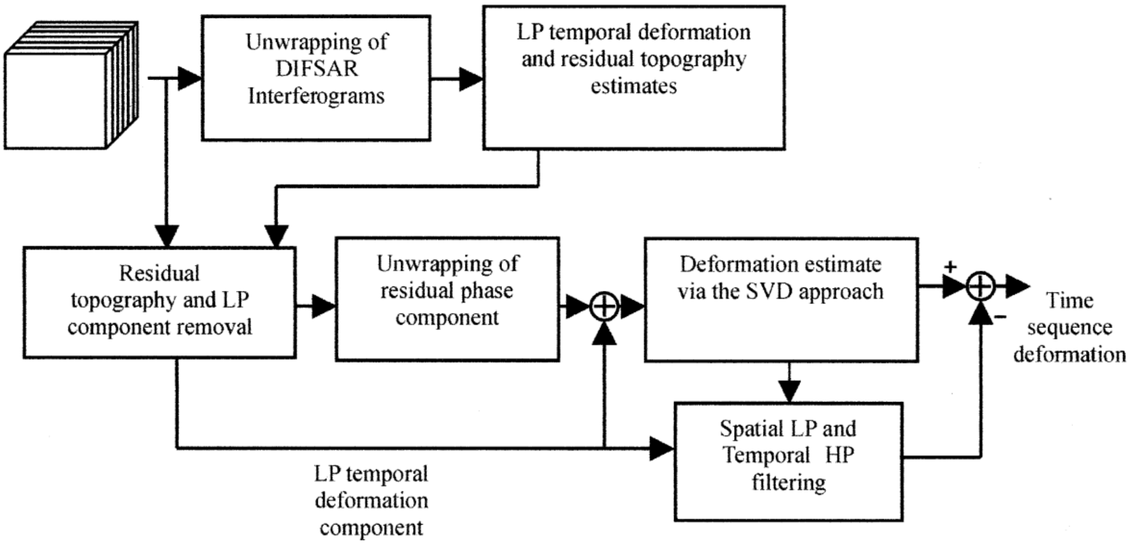


*Figure 1-5 - Block diagram of the SBAS algorithm*

- *Input data*

Set of SAR SLC data captured on interferometric conditions

- *Algorithms*
    - Co-registration
    - Interferogram generation
    - Filtering and coherence estimation
    - Phase unwrapping
    - Re-flattening
    - SVD inversion
    - Atmospheric effects filtering
    - Geocoding
- *Tools*

SARscape

- *Output product*
    - DEM in raster (TIFF) format
    - Terrain displacement velocity in raster (TIFF) format

### 3.1.4.2 Validation

The described algorithm has been implemented in SARscape software for several years, and it has been used in different commercial projects successfully. Multiple references about algorithm validity and accuracy can be found (Necula *et al*., 2017; Vassilevaa *et al*.,2017; Singh *et al.,* 2005; Yamane *et al.,* 2008; Deo *et al.,* 2014; Pandit *et al.,* 2014). From this last one, we extracted a plot to show the accuracy obtained by the algorithm in a mountainous area (Indian Himalayas) using TanDEM-X data, with an RMSE of 8.2 meters (Figure 3-6).

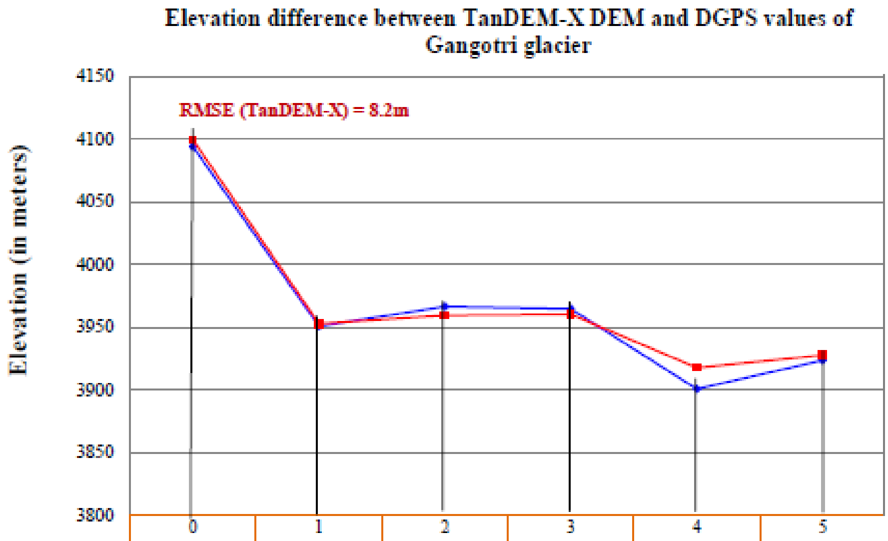


| | 0 | 1 | 2 | 3 | 4 | 5 |
|---|---|---|---|---|---|---|
| Observed (MSL) in meters | 4094,34 | 3950,95 | 3966,65 | 3964,66 | 3900,91 | 3923,71 |
| TanDEM-X (MSL) in meters | 4099,82 | 3953 | 3959,5 | 3960,39 | 3917,73 | 3927,9 |
| TDX(MSL)-Obs(MSL) | 5,477 | 2,046 | 7,152 | 4,272 | 16,818 | 4,184 |

*Figure 3-6 - Elevation values obtained through DGPS and TanDEM-X DEM for Gangori glacier (0 to 5 – Ground observation points)*

### 3.1.4.3 Application range and Maturity

The algorithm is mature, as it has been used and tested for years. In general, it can be used to generate DEM in any kind of terrain, but high slope and vegetation areas use to reduce SAR signal's coherence and decrease interferometry's accuracy.

## 3.1.5 References


Almeida L.P., Almar R., Bergsma E., Berthier E. Baptista P., Garel E., Dada O., Alves B, 2019. Deriving High Spatial-Resolution Coastal Topography From Sub-meter Satellite Stereo Imagery, Remote Sensing, 11(5), 590, doi:10.3390/rs11050590

Baran I., Stewart Mike P., Kampes Bert M., Perski Z., Lilly P.: "A Modification to the Goldstein Radar Interferogram Filter", IEEE Transactions on Geoscience and Remote Sensing, Vol. 41, No. 9, September 2003

Berardino P., Fornaro G., Lanari R., Sansosti E.: "A New Algorithm for Surface Deformation Monitoring Based on Small Baseline Differential SAR Interferograms", IEEE Transactions on Geoscience and Remote Sensing, Vol. 40, No. 11, November 2002

Capaldo P., Fratarcangeli F., Nascetti A., Pieralice F., Porfiri M., Crespi M., 2014 "Land applications of radar remote sensing. Chapter6. High resolution radargrammetry – 3D terrain modeling"

Choi J., Lee C., Won J., 2007 "DEM Generation over Coastal Area using ALOS PALSAR Data - Focus on Coherence and Height Ambiguity". Korean journal of remote sensing, Vol. 23, No. 6, pp.559-566

Costantini M.: "A novel phase unwrapping method based on network programming". Geoscience and Remote Sensing, IEEE Transactions on, May 1998, 36(3), pp. 813 - 821

Deo R., Rao "Vertical Accuracy Assessment of TanDEM-X DEM over Indian Test Areas" EUSAR 2014; 10th European Conference on Synthetic Aperture Radar

ESA TM-19: "InSAR Principles: Guidelines for SAR Interferometry Processing and Interpretation"

Ghulam A., Amer R., Ripperdan R.: "A filtering approach to improve deformation accuracy using large baseline, low coherence DInSAR phase images", Paper presented at IGARSS 2010

Göblirsch W., Pasquali P.: "Algorithms for calculation of digital surface models from the unwrapped interferometric phase". Proceedings of IGARSS 1996, pp. 656–658

Goldstein R.M., Werner C.L.: "Radar Interferogram Filtering for Geophysical Applications". Geophys. Res. Lett., 25(21), 4035–4038

Gruen A., 1985, Adaptive Least Squares Correlation: A powerful Image Matching Technique. South Africa Journal of Photogrammetry, Remote Sensing and Cartography, 14 (3), pp. 175-187

Gruen A., Zhang L., 2003. Automatic DTM Generation from TLS data. Optical 3-D Measurement Techniques VI, Vol. I, Zurich, pp. 93-105

Gruen A., Zhang L., 2004. Automatic DSM generation from linear array imagery data. Int. Archives of the Photogrammetry, Remote Sensing and Spatial Information Sciences, Istanbul, Turkey, Vol XXXV, Part B3, pp. 128-133

Hong S., Won J., 2006 "ERS-ENVISAT cross-interferometry for coastal DEM construction"

Meijering E., M. Unser, A Note on Cubic Convolution Interpolation, IEEE Transactions on Image Processing, Vol. 12, No. 4, April 2004

Milillo P., Rignot E., Rizzoli P., Scheulch, Mouginot J., Bueso-Bello J., Prats-Iraolla (2019). Heterogeneous Retreat and ice melt of Thwaites Glacier, West Antarctica. Science Advances, DOI: 10.1126/sciadv.aau3433

Monti Guarnieri A., Cafforio C., Guccione P., Nüesch P., Small D., Meier E., Pasquali P., Zink M., Desnos Y. L."Multi-mode ENVISAT ASAR Interferometry: Techniques and Preliminary Results". Proceedings of EUSAR Conference 2002

Monti Guarnieri A., P. Guccione, P. Pasquali, and Y.L. Desnos: "Multi-mode ENVISAT ASAR interferometry: Techniques and preliminary results, IEEE Proceedings on Radar, Sonar and Navigation, Vol. 150, No. 3, June, 2003

Necula N., Niculiţă M., Tessari G., Floris M.: « InSAR analysis of Sentinel-1 data for monitoring landslide displacement of the north-eastern Copou hillslope, Iaşi city, Romania" Proceedings of the Romanian Geomorphology Symposium 33rd edition, 2017

Nikolakopoulos K., Kyriou A., Charalampopoulo V., 2015 "DSM generation from Sentinel and COSMO-SkyMed data using interferometry and radargrammetry: A case study from Mykonos, Greece", Proceedings of SPIE - The International Society for Optical Engineering 9535, DOI: 10.1117/12.2193977

Pandit A., Ramsankaran R., Rao Y.S. "Generation and Validation of the Interferometric SAR DEMs from TanDEM-X data for Gangotri and Hamtah Glaciers of Indian Himalayas" Procedia Technology Volume 16, 2014, Pages 793-805

Reigber A., Moreira J.: "Phase Unwrapping by Fusion of Local and Global Methods". Proceedings of IGARSS'97 Symposium, 1997

Singh L., Westen C.J., Champati Ray P.K., Pasquali P. "Accuracy assessment of InSAR derived input maps for landslide susceptibility analysis: a case study from the Swiss Alps" Landslides (2005) 2: 221. https://doi.org/10.1007/s10346-005-0059-z

Small D., Pasquali P., Fuglistaler S.: "A Comparison of Phase to Height Conversion Methods for SAR Interferometry". Proceedings of IGARSS 1996 – Lincoln, Nebraska – USA – 27-31 May 1996

Vassilevaa M., Tonoloa F.G., Riccardi P., Lecci D., Boccardo P.: "Satellite SAR interferometric techniques in support to emergency mapping" European Journal of Remote Sensing, Vol. 50, No. 1, 2017

Yamane N., Fujita K., Nonaka T., Shibayama T., Takagishi S. "Accuracy evaluation of DEM derived by TerraSAR-X data in the Himalayan region" The International Archives of the Photogrammetry, Remote Sensing and Spatial Information Sciences. Vol. XXXVII. Part B7. Beijing 2008

Yu J.H., 2011 "Interferometric Synthetic Aperture Radar and Radargrammetry for Accurate Digital Elevation Model Generation in New South Wales, Australia" Thesis at the University of New Wales"

## 3.2 ALGORITHM GROUP 2: WATERLINE AND CREEK EDGE DETECTION

### 3.2.1 Introduction

Water lines are a key indicator for almost all coastal types. It is relevant for beaches as well as for the morphological assessment of intertidal flat dynamics. Therefore, we present here a number of different approaches and may select different ones for the different coastal types. The water line indicator is easily retrievable from both optical and SAR data, since the water surfaces exhibit radiometric signatures typical and different from other components of the coastal environment.

Although simple to extract, the water line is dependent on the tidal stage and swell conditions. Therefore, to infer relevant shoreline positions from the water line, it is necessary to define a cautious strategy for image acquisition. It is recommended to use high-tide or low-tide images only during calm weather conditions. Composite images based on time-series can also be used to minimize the impact of waves and tide. Indeed, in microtidal regions, the impact of tide level has a fairly low incidence on the water line location. If the water line is extracted from Sentinel-2 imagery the impact is probably marginal. However, it should be considered when using very high-resolution data.

These strategies must be considered whatever the extraction methods detailed hereafter.

Indeed, the waterline is a good proxy to identify the middle of the swash zone. In the Requirement Baseline, the middle of the swash zone is only required in microtidal regions, where this indicator is expected to be efficiently retrieved from an image time-series or from image composites as described below (algorithm 2a).

### 3.2.2 State-of-the-art

There are several techniques for delineating shorelines for change assessment, however, most studies use photogrammetry/satellite data and spatial analysis techniques (Evadzi et al., 2017; Appeaning Addo, Walkden, and Mills, 2008; Jayson-Quashigah, Appeaning Addo, and Kufogbe, 2013; Vos et al., 2019). Other techniques and data types utilized for quantifying beach erosion/shoreline changes includes storm-induced beach change model (Wise, Smith, and Larson, 1996), Bruun Rule (Bruun, 1962), Hallermeier equation (Hallermeier, 1981), shoreline evolution model (Patterson, 2009; Robinet et al., 2018), and shoreline response model (Huxley, 2009). Although these alternative methodologies to satellite/photogrammetry also make use of observations, apart from the reliability of each of the method itself, the suitability of the method also depends on the availability, spatial extent, and timescale of data.

Except for photogrammetry, which records historical coastal changes, the other methods are based on a combination of models and data, which are more useful when trying to estimate hazard extent where there is limited historical information.

Although shoreline/coastline definition over the years been debated because of the dynamic nature of coasts (Alves, 2007; Bird, 1985; Boak and Turner, 2005), the shoreline definition referred to as the ‘‘wet–dry’’ line, also referred to as the high water line, along the coast has been the most widely used definition for shoreline mapping because it can be identified both on images and physically in the field (Crowell, Leatherman, and Buckley, 1991; Dellepiane, De Laurentiis, and Giordano, 2004).

Several remote sensing researchers have worked on the topic of coastline extraction, firstly using SAR amplitude (Lee, 1990; Descombes et al., 1996; Niedermeier et al., 2000; Baghdadi et al., 2004) and then exploring capabilities of InSAR coherence analysis techniques (e.g. Schwabisch et al., 2006; Dellepiane et al., 2004; Wendleder et al., 2013). Albeit of the theoretically large backscattering difference in between land (bright) and water (dark), they collectively found noise effects (the water surface being frequently wind-affected, and effect of shallow waters) to be quite disturbing for automatic waterline extraction, thus exploring several approaches and filtering techniques to improve their differentiation. Another option to improve the discrimination water-land would be the use of polarimetric SAR (Wu et al., 2018). SAR images with HH polarization seem to be the most appropriate to discriminate coastline. Full polarized data can also be used to perform a polarimetric decomposition that will provide information about the degree of volume scattering, surface scattering and double bounce found on the terrain allowing a land-water classification (Gurreonero Robinson et al., 2013). Other discrimination measures derived from full polarimetric data have been proposed, as correlation between cross-polarization and co-polarization images, to improve separability land-water (Nunziata et al., 2016). The recently published paper by Schmitt et al. 2019 addresses the SAR state-of-the-art. Recently, the authors experimented an original TanDEM-X InSAR mono-static data mode "in pursuit" (both satellites flying with a larger spatial baseline and temporal baseline of 10 s) for land-water segmentation with the objective of obtaining denoised information and a better discrimination of both amplitude and coherence images. One dedicated case for water line detection is the application in intertidal flats to identify the dry-fallen flat surfaces and separate them from tidal creeks. Investigations in intertidal flat areas are based on both – optical and SAR data. Differentiation between water areas and dry-fallen intertidal flats is done by band ratios and linear spectral unmixing for the German Wadden Sea (Brockmann & Stelzer, 2008). The application of SAR data for the same question has been conducted by Gade & Melchionna 2016 and also the combination of both techniques, e.g. van der Wal 2005.

### 3.2.3 Algorithm 2ai - Water line detection using band ratios

#### 3.2.3.1 Algorithm Description

Evadzi *et al.* 2017, Appeaning Addo, Walkden, and Mills, 2008 and several coastal researchers argue that not only does band combination of satellite images provides the best atmospheric penetration and helps visualize Coastlines and shores but also by the application of band ratios helps to delineate shorelines along with the Wet-Dry line definition. Evadzi *et al.,* 2017 extracted historical shorelines for change assessment in Ghana, by performing Landsat data resolution standardization, histogram threshold and automatic shoreline extraction using ENVI classic software to separate the land and water based on band ratios (b2/b5 for Landsat 5 data).

The proposed algorithm is focused on band ratio and histogram threshold. This is applied to Sentinel-2 and Landsat-8 data; the later used for validation of the algorithm. The Sentinel-2 data is resampled to 10m whereas the Landsat-8 data is resampled to 15 m after conversion of the data's at-sensor radiance to at-sensor reflectance values.

Shorelines generated from Landsat data will not be at the exact location compared to those generated from sentinel-2 products mainly because of spatial resolution differences. However, the shorelines generated from both sources (based on the same expression) must represent the exact wet-dry lines that can be observed on the respective images as well as on the field.

Because of this capability, long term change detection can be computed using several data sources if the uncertainties such as positional/tidal changes accuracy, digitization uncertainty (e.g. if derived from orthophotos), as well as image resolution uncertainties, can be measured and applied as weights to the shorelines before the computation of change rates (Evadzi *et al.,* 2017).

- *Input data*

Sentinel-2 and Landsat-8 products were used for the delineation of the shoreline based on the water-line definition and band ratio approach explained above.

- *Algorithms*
    - Conversion of Landsat-8 product's at-sensor radiance values to at-sensor reflectance values.
    - Resample Sentinel-2 product to 10m and Landsat-8 to 15 m.
    - Compute the Wet-Dry Line from Sentinel-2 using the bands math (b8/b2), and the corresponding bands (band5/band2) to compute the shoreline for the Landsat-8 product.
    - Threshold for shoreline (1 >= Wet-Dry Line >= 0.9). This threshold is identified to be a good threshold for delineation of the shoreline as it does not only delineate the wet-dry line (Figure 3-7) but also minimizes the selection of mixed pixels that do not reflect the wet-dry shoreline (Figure 3-8); '0.5 <= shoreline (more mixed pixels) <= 0.9').
    - Preform Arithmetic Mean 3x3' to smoothing the shoreline.

- Polygonization of the mask to generate vector data.

- *Tools*

SN SNAP, QGIS, ArcGIS, DSAS

- *Output product*

Figure 3-8 shows shoreline extracted from sentinel-2 images after the water-line definition and band ratio approach explained above.


*Figure 3-7 - Automatic shoreline delineation from Sentinel-2 Image (data ref. date: 08-04-2019).*


*Figure 3-8 - The impact of thresholds on shoreline delineation from Sentinel-2 Image (data ref. date: 25-04-2019).*

### 3.2.3.2 Validation

The application of the algorithm (with the same threshold) works well for the generation of the wet-dry shoreline on both Sentinel-2 and Landsat-8 products. This is also expected to work for other satellite products that have similar corresponding bands. Figure 3-9 shows the delineated shoreline from Landsat-8 plotted on Sentinel-2 RGB image and shoreline for the same period. Although the Landsat-8 shoreline aligns with the Sentinel-2 shoreline at some places, there are slight shifts at some areas. This is expected mainly as a result of product resolution differences. If different products are to be used for historical rate of change computation, it is therefore important that the uncertainties must be accounted for and applied as weights to the respective shorelines.

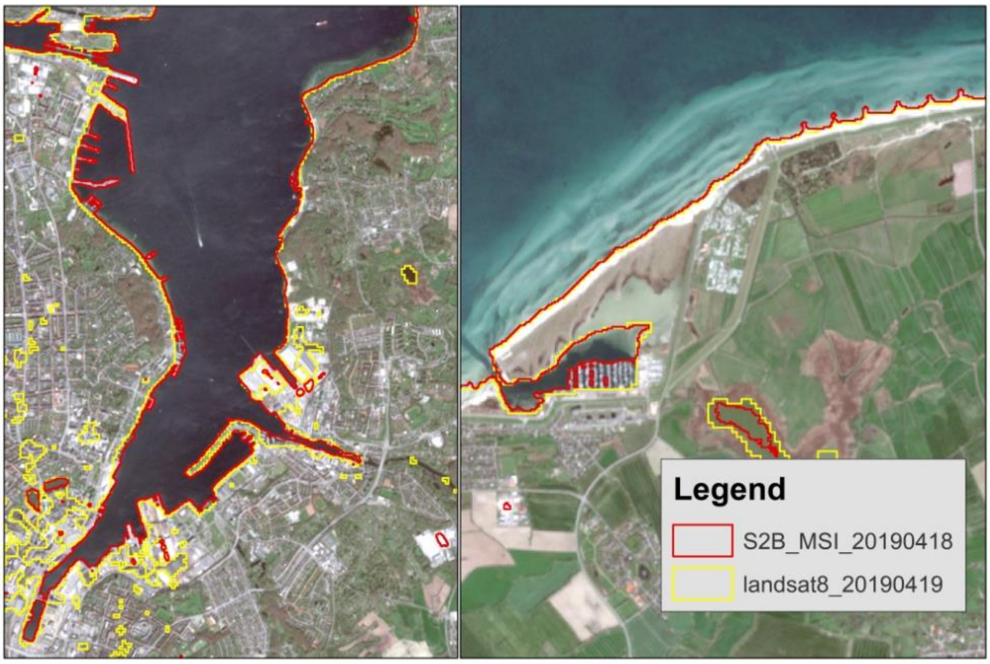


*Figure 3-9 - Different shorelines extracted from 2 sentinel and Landsat8 products (18/19-04-2019).*

### 3.2.3.3 Application range and Maturity

Coastal areas are very dynamic and are affected by climatic, geological, changes in the supply of sand to the coast, and anthropogenic factors. Extreme events to seasonal changes including cloud and foreign objects over the shoreline can significantly influence the delineated shoreline. Figure 3-10 shows the likely impact of the aforementioned factors on the shoreline delineation at the shores of Kiel. Several publications reported a similar challenge for the delineation of the wet-dry line for deltaic regions because of how dynamic these regions are. Care must be taken when selecting a shoreline to generalize for a month.

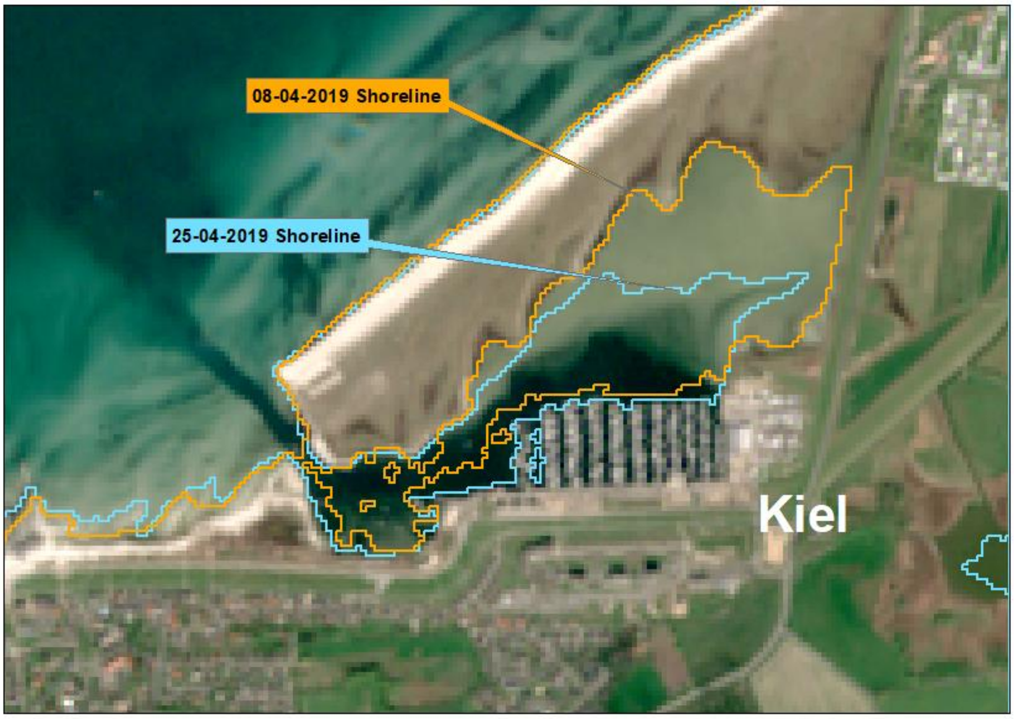


*Figure 3-10 - Different shorelines extracted from 2 sentinel images for 04-2019.*

### 3.2.4 Algorithm 2aii - Water line detection using NDWI

#### 3.2.4.1 Algorithm Description

- *Input Data*

The approach has been tested and validated for High Resolution optical data such as Landsat-8 and Sentinel-2 data, as well as Very HighResolution optical data such as Pleiades and SPOT-7.

- *Algorithms*

The water index and threshold-based water body mapping approaches have been developing ever since 1996, when McFeeters 1996 proposed the normalized difference water index (NDWI2), as a result of the following calculation between green and near-infrared (NIR) bands:

$$NDWI2 = (Bgreen - BNir)/(Bgreen + BNir)$$

Water bodies have positive values and non-water body features have negative values, while the index fails to suppress built-up structures signals efficiently. That was the case deriving from the 1st project phase results in the French and Greek test sites where this index was tested with the use of HR and VHR optical imagery. In particular, the algorithm has shown limited performance in defence structures and rocky areas in general, where the predicted waterline was not as accurate as on sandy locations and the extracted features were a mixture of water and built-up land noises.

In order to counter strike this algorithm limitation the modified normalized difference water index (mNDWI) was tested, particularly on areas with built-up structures, for to be deployed on 2nd project phase. According to the literature, mNDWI has introduced in 2006 by Xu for Landsat data, and made a change by replacing the NIR band with the shortwave-infrared (SWIR) band, which helped to remove the disturbances from built-up lands (Xu, 2006).

Meantime several other indicator configurations have also been tested for the 2nd project phase, that in literature are promising better results over man-made coastal structures (Zhou, 2017). In particular the following indexes have been tested:

- NDVI = (BNir − Bred)/(BNir + Bred)
- NDWI plus VI = 2.5 × (BNir − Bred)/(BNir + 6.0 × Bred − 7.5 × Bblue +1)
- NDPI = (BSWIR - Bgreen)/(BSWIR + Bgreen)
- WRI = (Bgreen + Bred)/(BNIR + BMIR)
- NDTI = (Bred - Bgreen)/(Bred + Bgreen)

Nevertheless, the results coming from all these error and trial tests proved that for the optical HR and VHR used the mNDWI is performing best over manmade structures. And since the results of NDWI for sandy areas were highly accurate we consider that this index will not be abandoned but a combination of indices can provide the best possible solution to the inaccuracies.

- Tools

Image processing tools used are either implemented on most image processing software (ENVI, ERDAS). Alternatively, they can also be found in OpenSource libraries.

- Outputs Products

Results carried out for shoreline extraction and shoreline change with time is shown in Figure 3-11. Vectors in shape format (or kml/kmz) are delivered.

*Figure 3-11 - Example of waterlines derived from SPOT-7 data using NDWI and mNDWI index, comparison with between predicted and observed waterline.*

### 3.2.4.2 Validation

According to Zhou et. al 2017 mNDWI-based algorithm have better performance of water body mapping in complex landscapes, while the NDWI had higher sensitivity for water body extraction in pure open surface water body regions, for Landsat-8 and Sentinel-2 data.

A GPS survey, of 45,1 km waterline took place from 30th September to 2nd October 2019, with the use of RTK GPS techniques (Real Time Kinematic, L1/L2 frequencies) and therefore by achieving a mean horizontal accuracy of a 2-3 centimetres for the collected data. These data are used for a soundful validation.

### 3.2.4.3 Application Range and Maturity

This approach with regards to water line extraction and borders between classes is considered as mature, as it has been applied on a worldwide basis. It applied to all sandy shorelines, whatever tidal range and wave exposure.

### 3.2.5 Algorithm 2aiii - Water line detection using AWEI (Automated Water Extraction Index)

#### 3.2.5.1 Algorithm Description

The Automated Water Extraction Index (AWEI) is yet another index-based methodology that can be used for waterline detection. The method was proposed and described by Feyisa *et. al* 2013 and it was further employed and tested by different other studies, such as the one of Bishop-Taylor *et. al* 2019, where multiple sites with different environmental characteristics were used in order to assess the accuracy of the method in comparison with other existing techniques (such as MNDWI).

- *Input Data*

The algorithm has been tested for Landsat 5, Landsat 8 and Sentinel 2 data. Visible and infrared (NIR and SWIR) wavelengths are required in order to compute de index, therefore can be applied to all types of imagery benefiting from such wavelengths.

- *Algorithms*

According to the authors, the aim of the AWEI formulation is to maximize separability of water and nonwater pixels through band differencing and by applying different coefficients. Two separate equations were proposed by the authors (Feyisa *et. al*, 2014): one that is specifically designed to perform better in situations where shadows are not a major problem and a second one, suitable for areas with shadow or other dark surfaces, which can be used in order to eliminate shadow pixels and improve water extraction. For the purpose of Space for Shore project, the first version will be used. This is defined by the following formula:

$$AWEI = 4 \times (\rho_{GREEN} - \rho_{SWIR1}) - 0.25 \times \rho_{NIR} + 2.75 \times \rho_{SWIR2}$$

where $\rho_{GREEN}$, $\rho_{NIR}$, $\rho_{SWIR1}$ and $\rho_{SWIR2}$ represent reflectance values for different regions of the electromagnetic spectrum.

The procedure for waterline extraction follows several steps, which are detailed hereafter:

- Applying atmospheric correction to all the images that will be used;
- Computing the AWEI index using multispectral satellite imagery (e.g. Sentinel 2, Landsat 5, Landsat 8);
- Applying the Otsu thresholding method (Otsu, 1979). This method is used to derive the best threshold value in order to separate the land pixels from the water pixels;
- Waterline indicator is derived at subpixel level and then, converted to vector line.

- *Tools*

The tools will be implemented by consortium members software and libraries such as GDAL, R and SNAP.

- *Outputs Products*

The output for this algorithm is a vector in shape format that contains the waterline position for a certain date.

Figure 3-12 presents the waterline position that was extracted from Sentinel 2 images using the AWEI index over different moments in time for Sulina – Sfantu Gheorghe site.

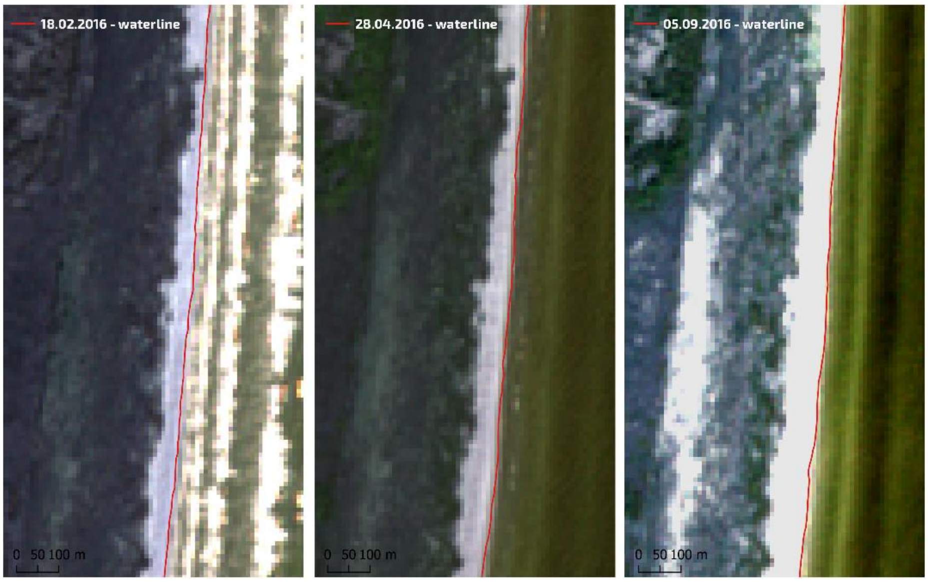


*Figure 3-12 - Example of waterlines derived from Sentinel 2 data using AWEI index over different moments in time*

### 3.2.5.2 Validation

The index accuracy was tested by Bishop-Taylor *et. al* 2019 for five different environments: sandy beaches, artificial shoreline, rocky shoreline, wetland vegetation and tidal mudflat, along the Australian coastline. The authors compared the results that were obtain using three different indices (NDWI, MNDWI, AWEI) and three different threshold methods. The subpixel waterline derived from AWEI index presented the highest accuracy for all five sample environments that were analyzed. Automated index thresholding approaches (e.g., Otsu) can be combined with subpixel methods to extract waterlines. The subpixel waterlines extracted from the 30 m resolution data using Otsu thresholding had an RMSE of 1.51 - 1.58 m (Bishop-Taylor *et. al,* 2019).

The algorithm was also validated for Sulina – Sfantu Gheorghe site. The validation activities consist of comparing the distance from in-situ GPS measurements with the waterline derived from MNDWI and AWEI indices. The results obtained using Sentinel 2 data showed that the indicator accuracy obtained using AWEI index is higher than the one obtained using MNDWI index (Figure 3-13).

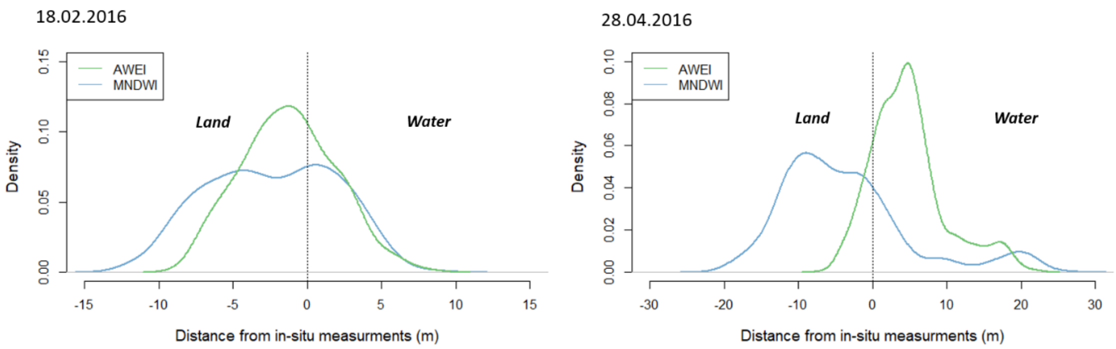


*Figure 3-13 - Distribution of the total number of differences between the in-situ GPS measurements and satellite derived waterline using AWEI and MNDWI indices for 2 different moments in time for Sulina – Sfantu Gheorghe site*

### 3.2.5.3 Application Range and Maturity

The results based on this algorithm, as tested by Bishop-Taylor *et. al* 2019 for five different environments, showed that the best accuracy was obtained using the AWEI index for waterline detection on sandy beaches, artificial shoreline, rocky shoreline, wetland vegetation and tidal mudflat. This algorithm was proved, by our initial estimations, to be highly accurate for Sulina – Sfantu Gheorghe site. It was applied on Landsat 8 and Sentinel 2 data and all the validation exercises showing the results will be reported in the following months.

### 3.2.6 Algorithm 2aiv - Water line detection using NDWI2

#### 3.2.6.1 Algorithm Description

- *Input Data*

The approach has been tested and validated for High Resolution optical data such as Sentinel-2 data and Very High Resolution such as Pleiades

- *Algorithms*

The upper waterline excursion represents the farthest location of water when it swashes on the beach during a period of time. Before getting the upper waterline excursion, waterlines must be computed for a set of close date imageries. The waterline detection method is based on Vos et al (2019). The steps are the following:

1. the image is georeferenced

2. a composite image is created by stacking a subset of the original bands and some indices (vegetation, water and soil)

3. a classification (random forest classifier) is performed on the image to detect the following classes: water, sand and other. To fit the random forest model, a training set has been digitized on a set of images

4. the NDWI2 index is computed

5. a threshold between NDWI2 sand pixel and NDWI2 water pixel is determined with the Otsu thresholding method

6. the marching square algorithm is used on the NDWI2 index with the previously determined threshold.

- *Tools*

python, orfeo toolbox, gdal, qgis.

- *Outputs Products*


*Figure 3-14 - Set of water lines extracted from Sentinel-2 images with NDWI2 and Otsu thresholding methods*

### 3.2.6.2 Validation

The validation step consists in measuring the average distance between a reference line and produced line from satellite data. First, the produced line is converted into point with a fixed distance (every 10m). Then the nearest distance from the point to the reference is line is computed. Finally, the error of each point is plotted and the average error is computed.

### 3.2.6.3 Application Range and Maturity

This approach with regards to water line extraction and borders between classes is considered as mature, as it has been applied on a worldwide basis. It applied to all sandy shorelines, whatever tidal range and wave exposure.

## 3.2.7 Algorithm 2e - Edge Detection tidal creeks using SAR

### 3.2.7.1 Algorithm Description

- *Input Data*

SAR data (single band) from one specific period, typically one calendar year.

Used are data from the Copernicus Sentinel-1 missions. The amount of data depends on the general availability (number of SAR sensors in orbit) and the effective acquisitions made around low tide in the area of interest.

- *Algorithms*

The satellites data used to produce indicators for the edges of tidal creeks has been processed using a processing chain (2E) with the following steps:

1.georeferencing
2. extraction of the AOI (8.567°-8.867°E 54.117°-54.300°N);
3. mosaicking of partly covering scenes;
4. identification of acquisitions made close to low tide;
5. generation of a data cube;
6. annual statistical analyses, including mean, standard deviation, minimum/maximum;
7. moving boxcar filter of size 11x11;
8. derivation of spatial gradients;
9. contrast enhancement

- *Tools*

All processing steps were performed using ESA's SNAP toolbox.

- *Outputs Products*

Annual maps of the Area of Interest with indicators for tidal creek edges. Large indicator values correspond to high likelihoods of creek edges, corresponding to strong signals in the SAR imagery.

#### 3.2.7.2 Validation

Results (indicators) are being validated in collaboration with the local end user (LLUR, Hans-Christian Reimers). An additional validation campaign in the course of a student excursion in May had to be cancelled, because of the travel ban

#### 3.2.7.3 Application Range and Maturity

The algorithm can be applied to SAR imagery of exposed intertidal flats of similar morphology (sediment composition) than in the Area of Interest. The most important constraint is that the data needs to be acquired close to low tide, i.e. at sufficiently low water level. An applicability to SAR data of different radar bands (primarily L-band) would have to be investigated, though such data is less frequently acquired. Maturity level is 3.

### 3.2.8 Algorithm 2f - Upper Swash Limit

#### 3.2.8.1 Algorithm Description

- *Input Data*

A set of waterlines in vector format.

- *Algorithms*

All the waterlines are combined and the farthest curve from the water is extracted as the upper waterline excursion. The manipulation consists in converting all the input features to polygon, merge the resulting features, converting back to polyline and extracting the onshore line manually.

- *Tools*

Arcgis

- *Outputs Products*

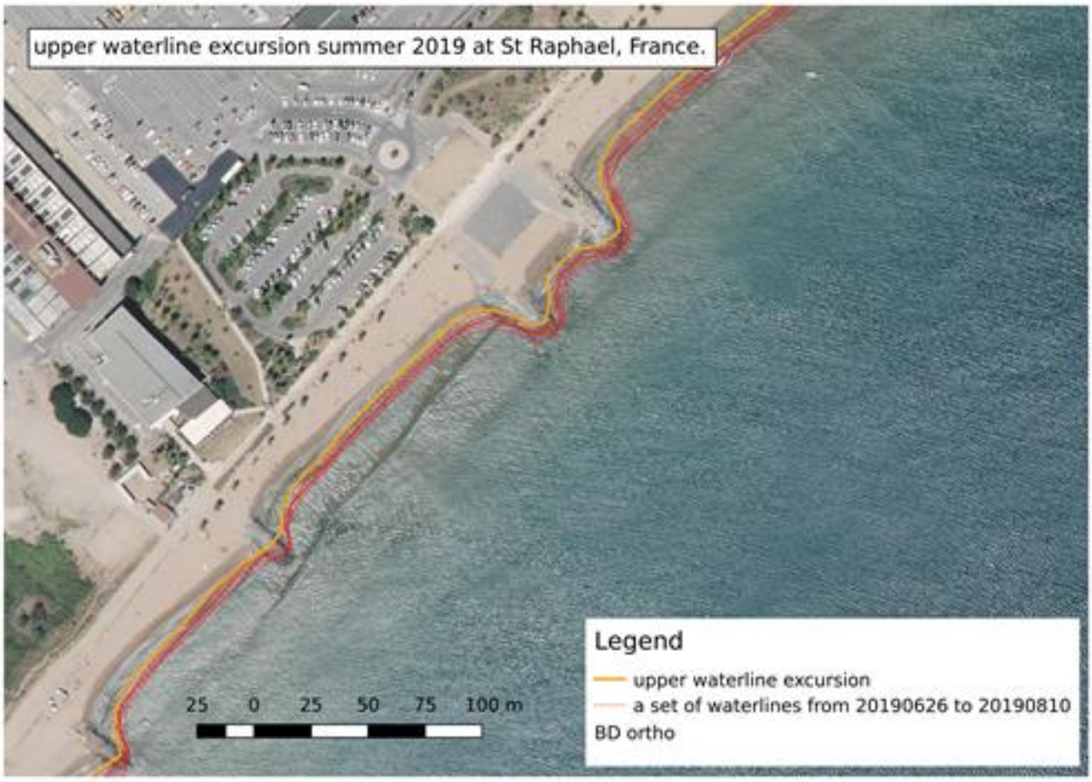


*Figure 3-15 - Upper swash limit computed from set of water lines*

### 3.2.8.2 Validation

The validation step consists in measuring the average distance between a reference line and produced line from satellite data. First, the produced line is converted into point with a fixed distance (every 10m). Then the nearest distance from the point to the reference is line is computed. Finally, the error of each point is plotted and the average error is computed.

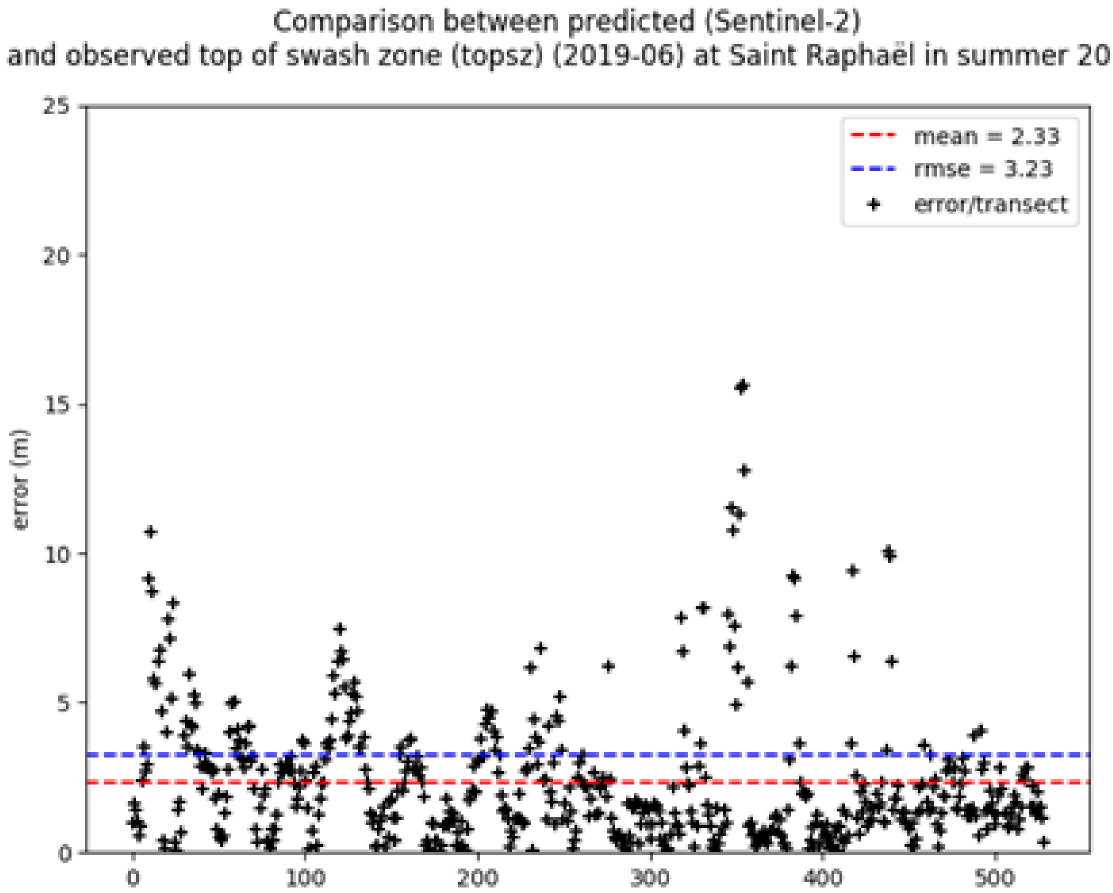


*Figure 3-16 - Mean and RMSE computation from distribution of errors measured for each transect*

### 3.2.8.3 Application Range and Maturity

This approach with regards to water line extraction and borders between classes is considered as mature, as it has been applied on a worldwide basis. It applied to all sandy shorelines, whatever tidal range and wave exposure.

## 3.2.9 Algorithm 2g - Waterline Extraction based on interferometric coherence from satellite SAR Images

### 3.2.9.1 Algorithm Description

- *Input Data*

This algorithm has been tested for ERS1/2, ENVISAT SLC data.

- *Algorithms*

This algorithm proposed for the extraction of the coastline is based on the creation of an average coherence between the pairs of SAR images of each year. Coherence information is always a powerful discriminant between land and sea (Dellepiane et al. 2004). The main idea of the algorithm is to detect the positions of large coherence value gradients in the correlation map which should reveal the boundaries between the high coherent land areas and the decorrelated water surface (Schwäbisch et al. 2014).

The first step for the extraction of the coherence image is derived from the correlation of the InSAR couple. In every pair, master image is set the first image of the year compared with all other dates. Interferometric coherence is an important indicator of suitability of the data scene obtained by a radar remote sensing system for the further processing and solving the final problem, i.e. generation of digital elevation model or terrain changes map. The coherence factor is calculated as the absolute value of the correlation coefficient between samples of two complex radar images (single-look data complex, SLC) got in the local windows

$$\hat{\gamma_0} = |\hat{\dot{\rho_0}}| = \frac{\Sigma \dot{z}_1(m,n) \cdot \bar{z}_2(m,n)}{\sqrt{\Sigma |\dot{z}_1(m,n)|^2 \cdot |\bar{z}_2(m,n)|^2}},$$

where z1(2) (m, n) is the SLC samples (¯z1(2) (m, n) are complex-conjugate samples) [2–5], ˆγ0 takes values in interval [0, 1], near-zero values correspond to areas of high or full decorrelation, which are not suitable for interferometric data processing (Sosnovsky et al. 2015). In order to reduce the noise, as the post-processing step, we perform multilooking and terrain correction. In case of ESA's ERS and Envisat sensors, the factor 5:1 (azimuth:range) or similar ratio between the factors is chosen to obtain approximately square pixels (20x20 m^2 for factors 5 and 1). Of course, the resolution decreases if multilooking is applied (SNAP).

In the second step, a stack of coherence layers is produced in order to calculate the average of each year. At the generated layer a filter is applied to reduce the speckle noise of the image (Lee Gamma window size: 13x13 target window size: 5x5).After the image is smoothed, an inspect of the histogram is applied on the area of the sea, in order to find a good threshold point to separate from the land. By applying the threshold, the image is classified into two types (sea–land binarization) for each pixel, and the boundary is extracted as the shoreline (Takashi et al. 2018). The produced layer is extracted as geotiff in order for further processing on GIS environment. Final the image is converted on vector data. Shoreline is generated by automatic algorithm.

- *Tools*

The tools will be implemented by consortium members software as SNAP, ArcGIS and QGIS.

- *Outputs Products*

The output for this algorithm is a vector in shape format that contains the waterline position for a certain date.

*Figure 3-17 - Example of waterlines derived from Sentinel 1 data over different moments in time*

### 3.2.9.2 Validation

For the validation will be used data from the land registry of Greece such as orthocorrected images and the digitized coastline from different years.

### 3.2.9.3 Application Range and Maturity

Coherence information has already been exploited successfully in landuse applications or for the purpose of forest/non-forest-discrimination. Forested areas, similar to water, mainly appear decorrelated in repeat-pass interferograms whereas agricultural and urban areas are characterized by medium to high correlation. (Askne *et al.* 1993, Wegmüller et al 1996, Schwäbisch *et al.* 2014).

## 3.2.10 Algorithm 2j - Decision tree classification based on band ratios and LSU

### 3.2.10.1 Algorithm Description

The classification of optical data for intertidal habitats and sediment distribution is based on a number of different decision trees. Dedicated decision trees are in place that focus on specific aspects of the intertidal flat areas, such as seagrass meadows and mussel beds, sediment distribution or the distribution of sediment and water areas, including remaining water ponds on the sediment surfaces. These decision trees, which use well defined features derived from optical data, will be used to characterize the intertidal habitats and their changes, in particular the morphological changes of intertidal creeks.

- *Input Data*

Each classification is based on a single acquisition of optical high resolution data from sensors onboard of Landsat-5, Landsat-8, Sentinel-2, SPOT-5-6-7, RapidEye. In order to detect the morphological characteristics and changes a long time series of classifications is required. The longest time series is available for Landsat series, starting with Landsat-5 MS, Landsat-8 ETM (1999-2003), Landsat-8 since 2013. Data availability is limited due to low tide constraints, but it has improved since the launch of Sentinel-2; having both – Landsat-8 OLI and Sentinel-2 MSI in parallel since 2015 and even with MSI-B since 2017. Until now, the intertidal flat classifications have been mainly applied to freely available data.

- *Algorithms*

A classification framework has been developed together with national park authorities to classify the intertidal flat areas of the Wadden Sea. The classification is based on a knowledge-based decision trees using different band combinations and linear spectral unmixing abundances (Müller et al., 2016). Examples of different decision trees are given in (Figure 3-18). For this specific product, the discrimination between sediment areas and tidal creeks (water) is needed. It also provides shallow water areas on the tidal flats (remaining water in depressions). Especially the shift of the tidal creeks and sediment flats is needed for assessing erosion processes in the Wadden Sea. Finally, the classification results are overlaid in order to visualise the shift of tidal creeks (Figure 3-19)

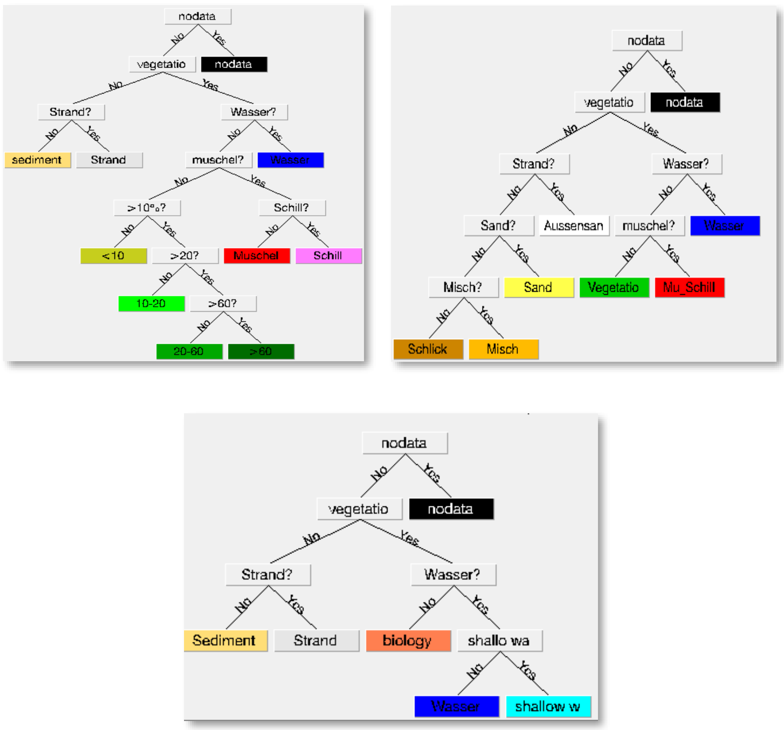


*Figure 3-18 - Examples of different decision trees for retrieving intertidal flat habitats and sediment distributions*

- Tools

SNAP and ENVI

- Output product

The output are classification results in raster format (Figure 3-19). They are overlaid for analysing the tidal creek changes. The products are used the assessment of erosion in the German Wadden Sea Test Sites (North Sea).

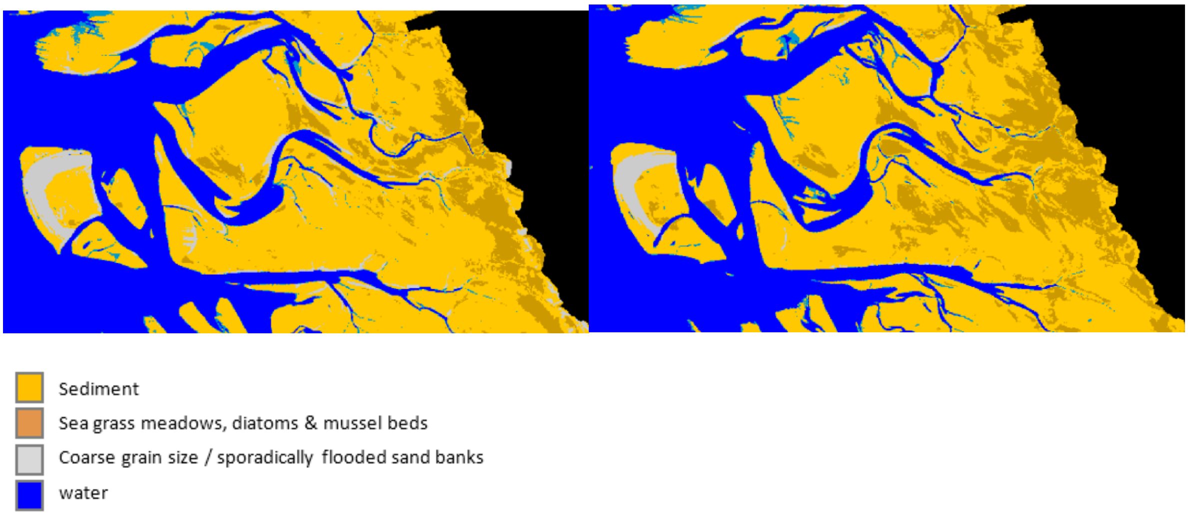


Figure 3-19 - *Classification of sediment flats and tidal creeks in 2015 (left) and 2016 (right*

As a next step, the land and water classes are used to determine the low-water line for the intertidal flat areas and creeks which is then converted to a vector data set. Overlay of different years show the movement of outer tidal flats and creeks (Figure 3-20).

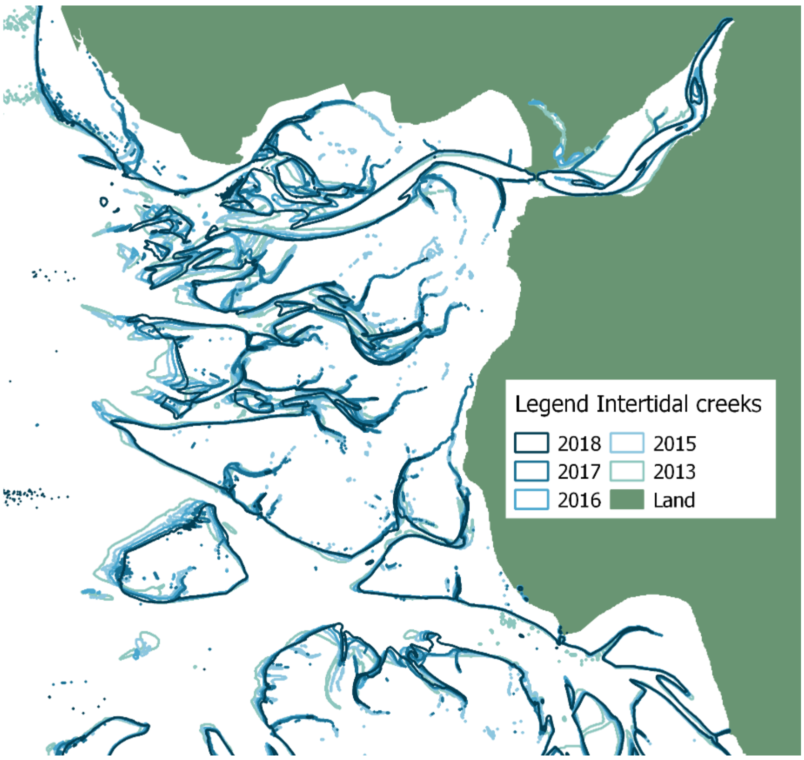


*Figure 3-20 - Changes of tidal creek positions between 2015 and 2018*

### 3.2.10.2 Validation

The classification of intertidal flat habitats, which is the basis of this application, has been validated in terms of sediment type and seagrass beds (Müller *et al*. 2016). However, the transition between water and land has only be validated against the original images, as the water level changes too fast due to tidal effects and cannot be evaluated in the field.

### 3.2.10.3 Application Range and Maturity

The method is strongly depending on the tidal phase and weather conditions during the images acquisition. Therefore, several images need to be analysed per period in order to get a representative distribution of the tidal creeks. Cloud free conditions and low tide are pre-conditions for good images and reduce the availability of suitable images. The situation has been improved since the launch of Sentinel-2.

The outcome, which needs to be applied to a longer time series will be used to observe the direction morphology changes and if creeks are approaching coastal areas or if large tidal basins undergo main changes (e.g. connection of tidal basins by tidal creek changes or break throughs. The identification of the trend is in focus for assessing the influence on coastal erosion. The more images are included, the better the expected results. As the water level is very variable, it needs to be demonstrated that the trend is still detectable. The accuracy of the trend detection will be very much influenced by the availability of suitable low tide images.

### 3.2.11 Algorithm 2k - In-land vegetation boundary method based on NDVI index

#### 3.2.11.1 Algorithm Description

- *Input Data*

Data used for this algorithm are Very High-Resolution optical data, in particular Pleiades and SPOT-7 imagery.

- *Algorithms*

The Normalized Difference Vegetation Index (NDVI) was developed in 1985 and represents the plant nitrogen assimilation condition and therefore its photosynthetic efficiency. NDVI index is an indicator which is used for the density of chlorophyll and leaf tissue and is expressed as following:

$$NDVI = (NIR - RED)/(NIR + RED).$$

NDVI gives values between −1 and +1, where vegetated areas in general yield high positive values and non-vegetated ground is found on the negative side.

The NDVI Index gives the difference between the healthy and unhealthy vegetation and assists in detecting the healthy vegetation boundary in the coastal area zone. According to Johansen et al., 2014 the NDVI values extracted from Landsat 7/ETM+ data over the peninsula of Nordenskiöld Land proved successful for coastal vegetation.

Also, Marzialetti *et al.* 2019, explored the potential of Sentinel-2 in capturing coastal dune natural vegetation types using a phenology-based mapping approach. It appeared that Sentinel-2 images confirmed their high potential for vegetation mapping, while the multitemporal analysis of NDVI provided complementary and useful information, proving its convenience even in complex vegetation mosaics, over Mediterranean areas.

- *Tools*

Image processing tools used are either implemented on most image processing software (ENVI, ERDAS). Alternatively, they can also be found in OpenSource libraries.

- *Output products*

Results carried out for coastal vegetation in-land boundary extraction is shown in Figure 3-21. Vectors in shape format (or kml/kmz) are delivered.

*Figure 3-21 - Example of vegetation boundaries derived from Pleiades data using NDVI.*

### 3.2.11.2 Validation

A GPS survey, of 45,1 km waterline took place from 30th September to 2nd October 2019, with the use of RTK GPS techniques (Real Time Kinematic, L1/L2 frequencies) and therefore by achieving a mean horizontal accuracy of a 2-3 centimetres for the collected data. These data are used for a soundful validation.

### 3.2.11.3 Application Range and Maturity

This approach with regards to vegetation line extraction and borders between classes is considered as mature, as it has been applied on a worldwide basis.

## 3.2.12 References

Appeaning Addo K., Walkden M., Mills J.P., 2008. Detection, measurement and prediction of shoreline recession in Accra, Ghana. ISPRS Journal of Photogrammetry and Remote Sensing, 63(5), 543–558. doi:10.1016/j.isprsjprs.2008.04.001

Alves M.V.M., 2007. Detection of Physical Shoreline Indicators in an Object-Based Classification Approach: Study Case: Island of Schiermonnkoog. Enschede, The Netherlands: The International Institute for Geo-Information Science and Earth Observation, Master's thesis, 53p

Askne J., Hagberg J. 1993, Potential of Interferometric SAR for Classification of Land Surfaces, Proc. IGARSS'93, Tokyo, 985-987

Baghdadi N., Gratiot N., Lefebvre J.P., Oliveros C., Bourguignon A. "Coastline and mudbank monitoring in French Guiana: contributions of radar and optical satellite imagery" Can. J. Remote sensing, Vol. 30, No. 2, pp. 109-122, 2004

Baselice F., Ferraioli G., 2013. Unsupervised coastal line extraction from SAR Images, IEEE Geoscience and Remote Sensing Letters, 10, 1350-1354

Bird E.C.F., 1985. Coastline Changes: A Global Review. Chichester, U.K.: Wiley, 219p

Bishop-Taylor R., Sagar S., Lymburner L., Alam I., Sixsmith J., 2019. Sub-Pixel Waterline Extraction: Characterising Accuracy and Sensitivity to Indices and Spectra. Remote Sens., 11, 2984

Boak E.H.,Turner I.L., 2005. Shoreline definition and detection: A review. Journal of Coastal Research, 21(4), 688–703. doi:10.2112/ 03-0071.1

Breiman L., 2001. Random Forests. Mach. Learn. 45, 1 (October 1 2001), 5–32. DOI:https://doi.org/10.1023/A:1010933404324

Brockmann C., Stelzer K., (2008). "Optical Remote Sensing of Intertidal Flats", in "Remote Sensing of the European Seas", V. Barale and M. Gade (Eds.), Springer, Heidelberg, pp. 117-128

Bruun P., 1962. Sea-level rise as a cause of shore erosion. Journal of the Waterways and Harbors Division, 88(1), 117–132

Canny J., 1986. A computational approach to edge detection", IEEE Transactions on Pattern Analysis and Machine Intelligence, vol 8, pages 679–714

Crowell M., Leatherman S.P., Buckley M.K., 1991. Historical shoreline change: Error analysis and mapping accuracy. Journal of Coastal Research, 7(3), 839–852

Dellepiane S., de Laurentiis R., Giordano F., 2004. Coastline extraction from SAR images and a method for the evaluation of the coastline precision. Pattern Recognition Letters, 25(13), 1461–1470. doi:10.1016/j.patrec.2004.05.022

Descombes X., Moctezuma M, Maitre H., Rudant JP (1996) Coastline detection by a markovian segmentation on SAR images, Signal Processing, 55, 123-132

Evadzi P.I., Zorita E., Hünicke B., 2017. Quantifying and predicting the contribution of sea-level rise to shoreline change in Ghana: information for coastal adaptation strategies. Journal of Coastal Research, 33(6), pp.1283-1291

Feyisa G.L., Meilby H., Fensholt R., Proud S.R., 2014. Automated Water Extraction Index: A new technique for surface water mapping using Landsat imagery. Remote Sens. Environ., 140, 23–35

Gade M., Melchionna S., 2016: Jint Use of Multiple Synthetic Aperture Radar Imagery for the Detection of Bivalve Beds and Morphological Changes on Intertidal Flats, Estuar. Coast. Shelf Sci., 171, 1-10, doi:10.1016/j.ecss.2016.01.025

Gurreonero Robinson D. A., Bijker W., Tolpekin V. A., 2013. Shoreline Detection Using TerraSAR-X Quad Polarization Mode. The International Hydrographic Review, 10

Hagenaars G., de Vries S., Luijendijk A., de Boer W., Reniers A., 2018. On the accuracy of automated shoreline detection derived from satellite imagery: A case study of the sand motor mega-scale nourishment, Coastal Engineering, 133, pp. 113-125, doi:10.1016/j.coastaleng.2017.12.011

Hallermeier R.J., 1981. A profile zonation for seasonal sand beaches from wave climate. Coastal Engineering, 4, 253–277

Hansen M. C. High-Resolution Global Maps of 21st-Century Forest Cover Change. Science 342, 850–853 (2013)

Huxley C., 2009. Shoreline Response Modelling Assessing the Impacts of Climate Change. http://www.coastalconference.com/ 2009/papers2009/Chris%20Huxley%20Full%20paper.pdf

Jayson-Quashigah P.N., Appeaning Addo K., Kufogbe S.K., 2013. Medium-resolution satellite imagery as a tool for monitoring shoreline change. Case study of the eastern coast of Ghana. In: Conley, D.; Masselink, G.; Russell, P., and

O'Hare T. (eds.), Proceedings from the International Coastal Symposium (ICS) 2013 (Plymouth, United Kingdom). Journal of Coastal Research, Special Issue No. 65, pp. 511–516. doi:10.2112/SI65-087.1

Johansen B., Tømmervik H., (2014). The relationship between phytomass, NDVI and vegetation communities Svalbard. International Journal of Applied Earth Observation and Geoinformation. 27. 20-30. 10.1016/j.jag.2013.07.001

Lee J.S., (1990) Coastline detection and tracing in SAR images, IEEE Transactions on Geoscience and Remote Sensing, 28, 662-668

Lorensen W. E., Cline H. E. (1987). Marching cubes: A high resolution 3D surface construction algorithm. ACM siggraph computer graphics, 21(4), 163-169

Luijendijk A., Hagenaars G., Ranasinghe R., Baart F., Donchyts G, Aarninkhof S. 2018. The State of the World's Beaches. SCIENTIFIC REPORTS | (2018) 8:6641| DOI:10.1038/s41598-018-24630-6

Marzialetti F., Giulio S., Malavasi M., Sperandii M., Gaia Teresa A., Acosta R., Carranza M., 2019. Capturing Coastal Dune Natural Vegetation Types Using a Phenology-Based Mapping Approach: The Potential of Sentinel-2. Remote Sensing. 11. 1506-1523. 10.3390/rs11121506

McFeeters S. K., 1996. The use of the Normalized Difference Water Index (NDWI) in the delineation of open water features. International Journal of Remote Sensing, vol. 17, n° 7, p. 1425-1432

Mentaschi L., Vousdoukas M.I., Pekel J.F., Voukouvalas E., Feyen L., 2018. Global long-term observations of coastal erosion and accretion, Scientific Report, 8(12876), doi: 10.1038/s41598-018-30904-w

Müller G, Stelzer K., Smollich S., Gade M., Adolph W., Melchionna S., Kemme L., Geissler J., Millat G., Reimers G., Kohlus J., Eskildsen K. (2016): Remotely sensing the German Wadden Sea – a new approach to address national and international environmental legislation. Environmental Monitoring and Assessment, 188(10), 1-17; DOI 10.1007/s10661-016-5591-x

Niedermeier A., Romaneessen E., Lehner S., 2000. Detection of coastlines in SAR images using wavelet methods, IEEE Transactions on Geoscience and Remote Sensing, 38, 605-616

Nunziata F., Buono A., Migliaccio M., Benassai G. "Dual-Polarimetric C- and X-Band SAR Data for Coastline Extraction" IEEE Journal of Selected Topics in Applied Earth Observations and Remote Sensing · May 2016

Otsu, N., A Treshold Selection Method from Gray-Level Histograms. IEEE Transactions on Systems, Man, and Cybernetics Vol. SMC-9, No. 1, https://doi.org/10.1109/TSMC.1979.4310076 (1979)

Otsu, N., 1979. A threshold selection method from gray-level histograms. IEEE transactions on systems, man, and cybernetics, 9(1), 62-66

Patterson D., 2009. Modelling the Shoreline Impacts of Richmond River Training Walls. http://www.coastalconference.com/2009/ papers2009/Dean%20Patterson%20Full%20paper.pdf

Pekel J.F., Cottam A., Gorelick N., Belward A.S., 2016. High-resolution mapping of global surface water and its long-term changes, Nature, 540(418), doi: 10.1038/nature20584

Pradhan B., Rizeei H.M., Abdulle A., 2018. Quantitative Assessment for Detection and Monitoring of Coastline Dynamics with Temporal RADARSAT Images. Remote Sens. 2018, 10, 1705

Robinet A., Idier D., Castelle B., Marieu V., 2018. A reduced-complexity shoreline change model combining longshore and cross-shore processes: The LX-Shore model. Environmental Modelling & Software, 109, 1-16, doi:10.1016/j.envsoft.2018.08.010

Schmitt M., Baier G., Zhu X.X., 2019. Potential of nonlocally filtered pursuit monostatic TanDEM-X data for coastline detection, ISPRS Journal of Photogrammetry and Remote Sensing, 8

Schwabisch M., Lehner S., Winkel N., 2006. Coastline extraction using ERS SAR interferometry, in Proceeding of 3rd ERS Symposium, 1049-1053

Schwäbisch M., Lehner S., Winkel N., 2014. COASTLINE EXTRACTION USING ERS SAR INTERFEROMETRY 3rd ERS SYMPOSIUM Florence 97 - Abstracts and Papers. https://earth.esa.int/workshops/ers97/papers/schwaebisc/361c.htm

Sosnovsky A., Kobernichenko V., 2015. Algorithm of Interferometric Coherence Estimation for Synthetic Aperture Radar Image Pair.In AIST (Supplement) (pp. 172-176)

Subramaniam S., Saxena M., 2011. Automated Algorithm for Extraction of Wetlands from IRS Resources at Liss III Data. ISPRS - International Archives of the Photogrammetry, Remote Sensing and Spatial Information Sciences, XXXVIII-8/W20, 193-198

Takashi F., Takashi O., 2018. Development of Shoreline Extraction Method Based on Spatial Pattern Analysis of Satellite SAR Images, Remote Sensing, Volume 10, Issue 9 , 1361

Van der Wal D., Herman P.M.J., Wielemaker-van den Dool A., 2005, Characterisation of surface roughness and sediment texture of intertidal flats using ERS SAR imagery. Remote Sens. Environ. 98 (1): 96-109

Vos K., Harley M.D., Splinter K.D., Simmons J.A., Turner I.L., 2019. Sub-annual to multi-decadal shoreline variability from publicly available satellite imagery. Coastal Engineering, 150, 160-174, doi:10.1016/j.coastaleng.2019.04.004

Vos K., Splinter K.D., Harley M.D., Simmons J.A., Turner I.L., 2019. CoastSat: a Google Earth Engine-enabled Python toolkit to extract shorelines from publicly available satellite imagery. Environmental Modelling and Software. 122, 104528

Wendleder A., Wessel A., Roth A., Breunig M., Martin K., Wagenbrener, 2013. TanDEM- water indication mask : generation and first evaluation results, IEEE Journal of Selected Topics in Applied Earth Observations and Remote Sensing, 6, 171-179

Wegmüller U., 1996. Land Applications Using ERS-1/2 Tandem Data, Proc. FRINGE '96, ERS Fringe Workshop Zürich

Wise R.A., Smith S.J., Larson M., 1996. SBEACH: Numerical Model for Simulating Storm-Induced Beach Change. Report 4. Cross-Shore Transport under Random Waves and Model Validation with SUPERTANK and Field Data. Vicksburg, Mississippi: U.S. Army Engineer Waterways Experiment Station, Technical Report CECR-89-9, 140p

Wu L., Tajima Y., Yamanaka Y., Shimozono T., Sato S. "Study on characteristics of SAR imagery around the coast for shoreline detection" Coastal Engineering Journal Volume 61, 2019 - Issue 2

Xu H., 2006. Modification of normalised difference water index (NDWI) to enhance open water features in remotely sensed imagery. International Journal of Remote Sensing 27,3025-3033. https://doi.org/10.1080/01431160600589179

Yan Z., Jinwei D., Xiangming X., Tong X., Zhiqi Y., Guosong Z., Zhenhua Z., Yuanwei Q., 2017. Open Surface Water Mapping Algorithms: A Comparison of Water-Related Spectral Indices and Sensors. Water, 9:256. https://doi.org/10.3390/w9040256

Yan Z., Jinwei D., Xiangming X, Tong X., Zhiqi Y., Guosong Z., Zhenhua Z., Yuanwei Q., 2017. Open Surface Water Mapping Algorithms: A Comparison of Water-Related Spectral Indices and Sensors. Water. 9. 256. 10.3390/w9040256

# 3.3 ALGORITHM GROUP 3: EXTRACTION OF SUBAERIAL MORPHOLOGICAL STRUCTURES AND CHANGES

## 3.3.1 Introduction

This section presents algorithms that are used to compute key indicators useful to assess the morphodynamics of different subaerial areas along the sandy and rocky coasts and to mitigate risks related to erosion processes. Attractive coastal areas are usually well urbanized with the building of expensive seafront, facilities and houses on top of coastal dunes and cliffs. Monitoring the dunes foot and the main cliff lines (foot and apex) is crucial for coastal stakeholders to anticipate the impact of erosion that can damage seriously these infrastructures and threaten the safety of coastal users. The knowledge of the beach width is also essential for coastal municipalities as it provides an indication on the recreational potential and attractiveness of their coastlines. This indicator is therefore often included in beach nourishment strategy. Although less widespread in end-user practices, the tracking of unusual and sudden low-amplitude vertical movements on top of cliff can also indicate a ground instability and warn of a likely and future landslide usually associated with dramatic impacts if not anticipated. The study of ground vertical movements on longer timescales (> annual timescale) can also reveal the existence of trends of gradual downward settling of the ground surface, called subsidence. Within deltaic environments this ground process, which can reach several centimetres per year in some places, leads to a continuous coastline retreat and higher exposure to marine flooding.

## 3.3.2 State-of-the-art

Linear features (dunes foot, cliff lines) extraction in coastal areas can be made following different approach. The simpler strategy relies on manually digitizing polylines (Hapke and Reid, 2007) from raw images, processed image where features are enhanced, DEMs or even combination of DEMs and images. The main advantages of this method are that:

- it can be performed using only basic tools from GIS software
- the operator digitizing the linear features can identify possible source of error and take a decision based on ground-truth knowledge that is sometimes nearly impossible to automate
- the outputs of the digitizing procedure are directly polylines and no post-processing is required before delivery to end-users

However, this approach includes some limitation. First, the operator requires an accurate knowledge of the study site to avoid subjective decision in digitizing (e.g. when the dune foot line starts be blurred due to accretion processes that sometimes occur). Second, this approach is really time consuming. While manually digitizing lines for few images is rather acceptable with production times expected to be of some hours to days, applying this procedure to a high number of dates and sites becomes totally inefficient.

To overcome these limitations, scientists and companies tend to develop automated tools (e.g. Hoeke *et al.,* 2001; Brzank *et al.,* 2005; Zarillo *et al.,* 2008; Liu *et al.,* 2009; Lafon *et al.,* 2010, 2014). However, some manual and site-specific operations are always necessary because of the high variability in shape and characteristics of coastlines worldwide. These manual operations included in these so-called semi-automated algorithms allow calibrating some coefficients used at different steps of the algorithm (e.g. kernel size for computing textural parameters, characteristic length scale of the dunes and cliffs present in the image or DEM, thresholds on metrics of ground slope or on texture or on reflectance).

To the author knowledge, there is no published references specifically dealing with coastal dune foot line extraction from satellite imagery, apart from the work of Lafon *et al.,* 2014 based on texture metrics, and also method based on multispectral image classification (Lafon *et al.,* 2010; Roche *et al.,* 2014). The dune foot is usually defined as the abrupt increase of slope observed at the transition between the upper beach (landward the berm) and the dune front (Boak and Turner *et al.,* 2005; Toure *et al.,* 2019). This cannot be detected directly from a satellite image. However, the transition between the beach and dune area is also marked by changes in surface reflectance and texture. Over the beach, the image reflectance is usually high and homogeneous while landward the dune face the reflectance can be lower and more heterogenous due to presence of vegetation and local shadows that typically appear in dune fields. The foredune face can also present a different spectral signature and typology compared to the upper beach. While extraction of a dune foot proxy from texture metrics requires VHR optical image, extraction from results of classifications applied to image reflectance signature and band ratios can also rely on HR image.

Studies focusing on coastal variability and in particular on the dunes system usually uses DEM (generated from DGPS or LIDAR topographic surveys or from photogrammetry that uses images taken from UAV, plane or satellite) to compute date-to-date changes in dune volume (e.g. Castelle *et al.,* 2015; O'Dea *et al.,* 2019; Laporte-Fauret *et al.,* 2019). The DEM can also be used to extract the dune foot by using a slope threshold calibrated with ground observation (e.g. Nahon *et al.,* 2019) or by using image processing methods for edge detection within raster of elevation (e.g. Richter *et al.,* 2013). Analysing the slope variability in the cross-shore direction, with the search of the location of the first maximal slope increase from the upper beach, can also allow us detecting the dune foot (e.g. Le Mauff *et al.,* 2018). However, except for coastal dunes suffering regular erosion events leading to a clear and sharp slope break, the transition between the upper beach and the dune face is sometimes blurred by sand sliding over the dune face to the dune base (Battiau-Queney *et al.,* 2003). In that case the dune foot can no longer be represented by a line but more by a 2-3-m wide buffer area (Guillén *et al.,* 1999). In case of coastal system undergoing accretion, the dune foot can even not be tracked rigorously, even by field works, as several embryo dunes form on the upper beach with vegetation usually developing on the top. These two morphodynamic processes represent potential source of errors in the detection of the dune foot from DEM, as only regular field works can check their occurrence in time and space. No any reference describing and validating methods for coastal dune foot extraction from satellite-image-derived DEM is found in the literature. Nevertheless, as production of coastal dune DEMs from optical spatial imagery using photogrammetry shows promising results (Almeida *et al.,* 2019), the detection of the dune foot from space based on elevation and slope data appears feasible.

Detection of cliff lines in coastal areas can be done in similar ways as for the dune foot detection. Seaward the cliff foot is usually found find a gently sloping rocky platforms intermittently covered by sand or shingle deposits. Landward the cliff foot starts the cliff face, which is essentially characterised large elevation gradients at least an order of magnitude higher than those found elsewhere in the coastal area. A large variety of morphologies along the cliff face are observed worldwide due to different lithologies and processes involved in the cliff dynamic. The upper boundary of the cliff face, called top, is delimited the strong reduction of the ground slope and the start of more morphologically stable areas where vegetation and urbanisation can develop. For cliffs relatively steep shadows are usually projected on the cliff face seaward the cliff top due to obstruction of sunlight. This occurs when the earth-projected sun location is located landward the cliff top and when the sun elevation is lower than the cliff slope. Similar to the dune foot extraction, supervised classifications can be applied to extract the cliff lines based on these specificities. However, the success of the classification and the further extraction of cliff lines is essentially site specific and requires to identify consistent proxy of these line. Both VHR and HR optical images can be used, although extraction based on HR data will allow to detect significant changes within the cliff only if large temporal period are considered (e.g. 10-20 years) or if the cliff change rate are high (1-10 m/year), which is rarely the case.

Several methodologies for cliff line extraction were developed in the last decades relying on LIDAR-derived DEM but using different approaches. For instance, Gomes-Pereira and Wicherson, 1999 applied image processing tools (mathematical operator) on rasterized DEM (elevation grid) to classify image pixels into 'slope pixel' or 'flat pixel'. Then, the cliff lines were assumed to be found at the boundary between the two classes of pixels and were identified by checking the 8-point neighbourhood of each pixels. Sui *et al.* 2002 also used image processing method (edge detection with the Canny operator) to a LIDAR-derived DEM transformed into a greyscale image. A more geometrically based approach exploiting the entire 3D information provided by the LIDAR measurements was addressed by Briese, 2004. It consists in fitting planes to the 3D point cloud and identifying intersections between two adjacent planes, which locate either the cliff foot line or the cliff top line. With the same idea, Brzank *et al*., 2005, extended this approach by locally fitting a surface described by the hyperbolic tangent function to the cliff DEM. Then, geometrical analyses are made on the modelled surface to locate the two maxima in surface curvature (one convex and one concave) in cross-shore direction, which corresponds to the cliff foot and top, respectively. These methods however may fail with increasing coastal complexity and presence of vertical perturbation in the DEM unrelated to the ground elevation such as vegetation and buildings. A different approach was proposed by Liu *et al*. 2009 who exploited directly the elevation data provided by the DEM along a series of adjacent and regularly spaced transects oriented perpendicular to the cliff face. They based their approach on the conceptual representation of the cliff mentioned above, which is that the variation of the slope along the elevation profile is commonly greater at the top and the base of the cliff than anywhere else along the profile. Still using a transect-based approach Palaseanu-Lovejoy *et al.,* 2016 introduced a new methodology that resolves easily the detection of the cliff foot and top along elevation profiles extracted from LIDAR-derived DEM. It even captures the presence of major irregularities along the cliff faces such as terrace that could represent a large source of error using previous methodologies.

For coastal managers, the beach width (Robertson *et al.,* 2007) usually refers to the cross-shore distance over which the beach is most of the time dry and then fully available to welcome recreational activities. For beaches experiencing a micro tidal range, the beach width can reasonably be approximated by the cross-shore distance between the upper limit of the beach – marked by the dune or cliff foot or the base of defence structures – and the instantaneous waterline or the line passing through the middle of the swash zone. For beaches experiencing a larger (macro/mega) tidal range, the use of the mean high-water line as the proxy of the seaward boundary of the beach width is more appropriate (Burroughs and Tebbens, 2008; Richter *et al.,* 2013, as it would limit the large horizontal fluctuations of this boundary that are associated with the daily water level fluctuations.

Differential SAR interferometry (Massonnet and Rabaute, 1993), allows measurements of land deformation very precisely with millimetre resolution. It has various applications in the fields of volcanology, cartography, coastal dynamics and land subsidence. By using large stacks of SAR images acquired over the same area, long deformation time series can be analysed using multitemporal differential SAR interferometry techniques. These coherent methods exploit either permanently coherent Persistent Scatterers (PSs) or temporally coherent Distributed Scatterers (DSs). PSs are typically artificial objects that reflect radar energy well such as metal structures and buildings. The PS methods that have been developed include the Permanent or Persistent Scatterer Interferometry (PSI). PSI provides a parametric estimation of the 3D location and velocity of each PS along the line of sight (LOS) connecting it to the satellite (Ferretti *et al.,* 2000; Ferretti *et al.,* 2001). Many such measurements are combined using PSI to produce highly accurate terrain motion maps. In urban areas where there is a prevalence of PSs, PSI allows analysis of even individual structures on the ground. The DS methods include algorithms such as SBAS. A DS object reflects lower radar energy compared to PSs and it usually covers several pixels in high resolution SAR images. These pixels exhibit similar scattering properties and can be used together for deformation estimation. SBAS estimates the deformation time series even in rural areas where the density of PSs is low (Berardino *et al.,* 2002), such as in low urbanized deltaic environments.

### 3.3.3 Algorithm 3c - Cliff line extraction using the cross-shore variation of the beach/cliff slope

#### 3.3.3.1 Algorithm Description

- *Input data*

This algorithm relies on the availability of a digital elevation model (DEM) that includes the cliff face and part of the subaerial domains seaward and landward the cliff face so as to have the cliff foot and apex within the DEM. The DEM can be computed from photogrammetry or stereo-radargrammetry using VHR optical images or from interferometry using VHR SAR images (see algorithm group 1 Section 3.1). The proposed algorithm for cliff foot extraction relies on a DEMs provided over a regular mesh.

The proposed algorithm is expected to require some tuning coefficient that surely will depend on the characteristic dimensions of the cliff system, such as the average cliff height and slope.

The proposed algorithm is expected to be able to detect automatically a reference line following locally the overall cliff face orientation that is used to define perpendicular transects along which the cliff foot and apex detection will be performed. However, if this part of the algorithm lacks robustness, it may be necessary to provide the reference line or the transects for each POC site.

- *Algorithms*

The main steps of the algorithm are presented in Figure 3-22 with blue, grey and yellow boxes indicating the main inputs, the sub-algorithms to be developed and the algorithm and sub-algorithm outputs, respectively. The overall idea is to detect the location of particular changes in slope combined with cliff elevation ranges along regularly-spaced transects locally perpendicular to the cliff face. Indeed, landward the sea the beginning of the cliff face is usually characterized by a strong increase of the slope at the cliff foot and a strong decrease at the cliff apex. Seaward the cliff foot and landward the cliff apex the slope is weak while in between the slope is high while. The first main step of the algorithm is to identify a line approximating the cliff face location from which perpendicular, regularly-spaced detection transects will be defined. Then, along each of these transect the cross-shore variability of the ground slope is analysed. In particular, inflexion points in the slope, which are characterized by the second derivative of the elevation equal to zero, are tracked as they might be the best proxy for transitions between the different coastal compartments. Here, only tests one real DEMs will allow robust implementation of this critical part of the algorithm. Existing methodologies (e.g. Liu *et al.,* 2009; Brzank *et al.,* 2005) for cliff lines detection will be investigated to support the algorithm implementation.

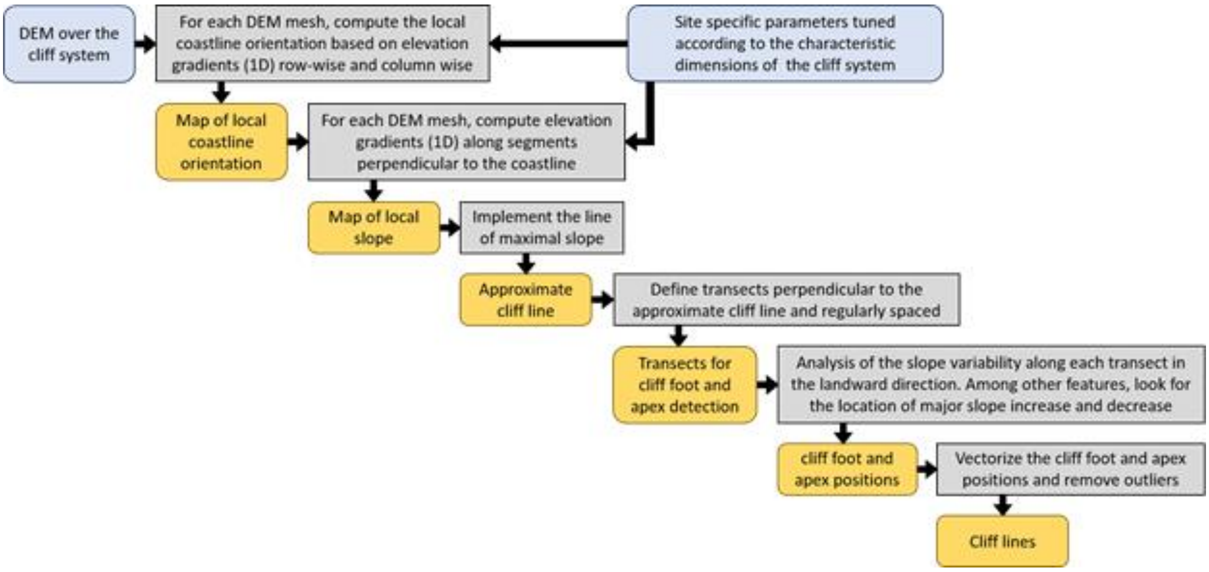


*Figure 3-22 - Methodology proposed to extract the cliff lines from DEMs*

- *Tools*

Python programming language.

- *Output product*

The outputs from this algorithm are vectors of cliff foot and cliff apex position


*Figure 3-23 - Cliff lines extraction from Pleiades images*

#### 3.3.3.2 Validation

As for the dune foot line extraction algorithm the maximal horizontal accuracy is expected to be of the order of the DEM resolution, with DEM horizontal resolution usually set to the double of the resolution of the original images. Thus, for a DEM perfectly well computed using Pleiades images of 0.5-m resolution the horizontal accuracy in dune foot detection would be of the order of 1 m. A lower accuracy is however likely as the image georeferencing of the images may not be totally perfect and mainly because slope break extraction from discrete elevation data can introduce errors.

#### 3.3.3.3 Application Range and Maturity

Coastal cliffs within Europe present a great variety of shapes in both the horizontal and vertical directions making nearly impossible to have a single automated algorithm applicable to all cliff geometries. Here, the proposed algorithm will be developed essentially for cliffs of simple geometry (e.g. relatively straight in top view, low ground slope seaward the cliff foot and landward the cliff top, no multiple detachments of the cliff in the cross-shore direction). The proposed algorithm also assumes that the cliff foot is always located seaward the cliff apex, which is not always true as for cliffs made of hard materials and suffering rapid wave-induced erosion at their base. In case the sea is directly in contact with cliff face within the EO data used to compute the DEMs, the cliff foot line detection with the proposed algorithm is no longer possible. Instead the line of contact between the sea and the cliff face may be a relevant proxy of the cliff foot line. The detection of the cliff apex is still possible as long as the cliff face (in contact with the sea) covers several meshes within the DEM. The maturity of the proposed algorithm is considered as low, though a first implementation within some weeks is likely reachable.

### 3.3.4 Algorithm 3d - Semi-automated linear feature extraction from DEM's

#### 3.3.4.1 Algorithm Description

Photogrammetric techniques have been used in the past for accurate 3D reconstructions- reconstitutions and specifically for extracting 3D point coordinates (X, Y, Z) as well as 3D lines. For this purpose, the appropriate image stereo pair must be available, while the extraction is a point-by-point process which in the past used to be manual. Following the development of analytical stereo-plotters this process became semiautomatic, while nowadays, with the availability of digital images and digital photogrammetric solutions, cost-effective almost-automated methods are widely offered for any visual-based measuring purpose. Though the photogrammetric production chain is almost automated, still human operators are required in the process by providing expertise not yet modelled by state-of-the-art photogrammetric suites.

- *Input data*

High resolution optical stereo-pair imagery will be used, in this case SPOT-7 stereo imagery with spatial resolution 1.5m acquired on 28/08/2019, on an on-the-sensor stereo mode. Meantime, Ground Control Points (GCPs) are needed in order to achieve the most accurate results of the bundle adjustment with RPC coefficients model. In this case GCPs are available for the Greek demonstration sites coming from existing orthomosaics (resolution 0.25m) with an accuracy RMSExy <0.35m.

- *Algorithms*

The first step of this is algorithm the restitution of orientation of the stereo-model, which in the case of HR and VHR optical satellite imagery it is done by deploying the RPC coefficients model approach. The whole process consists of calculating a mathematical model, which aims to restore a geometric relationship between the image and the object. This process of orientation of satellite imagery differs, in comparison, with the well-known process of aerial triangulation (which is based on the geometry of the central projection). The model used for high-resolution satellite imagery is the "Rational Function Model", which has attracted the interest of Photogrammetry and Remote Sensing due to the fact that some satellite imaging suppliers have adopted the Rational Function model as a replacement sensor model for image exploitation (Tao and Hu, 2002).

$$l_n = \frac{Num_L(U,V,W)}{Den_L(U,V,W)} \quad (1)$$

$$s_n = \frac{Num_S(U,V,W)}{Den_S(U,V,W)} \quad (2)$$

$$\begin{aligned} Num_L(U,V,W) &= a_1+a_2V+a_3U+a_4W+a_5VU+a_6VW+a_7UW+a_8V^2+a_9U^2+a_{10}W^2+a_{11}UVW \\ &+a_{12}V^3+a_{13}VU^2+a_{14}VW^2+a_{15}V^2U+a_{16}U^3+a_{17}UW^2+a_{18}V^2W+a_{19}U^2V+a_{20}W^3 \end{aligned} \quad (3)$$

$$\begin{aligned} Den_L(U,V,W) &= b_1+b_2V+b_3U+b_4W+b_5VU+b_6VW+b_7UW+b_8V^2+b_9U^2+b_{10}W^2+b_{11}UVW \\ &+b_{12}V^3+b_{13}VU^2+b_{14}VW^2+b_{15}V^2U+b_{16}U^3+b_{17}UW^2+b_{18}V^2W+b_{19}U^2V+b_{20}W^3 \end{aligned} \quad (4)$$

$$\begin{aligned} Num_S(U,V,W) &= c_1+c_2V+c_3U+c_4W+c_5VU+c_6VW+c_7UW+c_8V^2+c_9U^2+c_{10}W^2+c_{11}UVW \\ &+c_{12}V^3+c_{13}VU^2+c_{14}VW^2+c_{15}V^2U+c_{16}U^3+c_{17}UW^2+c_{18}V^2W+c_{19}U^2V+c_{20}W^3 \end{aligned} \quad (5)$$

$$\begin{aligned} Den_S(U,V,W) &= d_1+d_2V+d_3U+d_4W+d_5VU+d_6VW+d_7UW+d_8V^2+d_9U^2+d_{10}W^2+d_{11}UVW \\ &+d_{12}V^3+d_{13}VU^2+d_{14}VW^2+d_{15}V^2U+d_{16}U^3+d_{17}UW^2+d_{18}V^2W+d_{19}U^2V+d_{20}W^3 \end{aligned} \quad (6)$$

This model is based on polynomial coefficients and correlates the geographical coordinates of the object with the measured L, S coordinates. It is given by eighty coefficients (RPCs) and ten coefficients of scale and displacement. The model is in the form of two cubic equations of the coordinates of space. Separate rational functions are used to express the ratio of coordinates (L) and (S) (Equations 1 - 6).

The result of this model provides the restitution of image orientation and then a second step follows for extracting the DEM, which is based in the use of two families of matching methods:

i. Feature Based Matching

Feature Based Matching (FBM) is a matching strategy that is very robust. It only needs coarse approximations and is very fast. It has an accuracy of about 1/3 of a pixel. The matching process computes interest values in two images of a matching pair that describe the appearances of features. The matching process determines common features in the pair by means of the computed interest values.

ii. Least Squares Matching

Least squares matching (LSM) is a matching strategy that is very accurate, but better approximations are required, and it is considered rather slow in comparison to FBM. It is mostly used to refine points obtained from FBM. The accuracy is about 1/10 pixel. The matching process uses a mask created from one image and a template from the second image at a previously matched point. The mask is shifted on the template until the sum of squares of the gradients is minimized.

### 3.3.4.2 Validation

The results of algorithms are being validated through in situ GPS measurements, for this reason points lying on cliff foot and apex are being collected through an on-the-field survey, with an accuracy of 2-3cm. These collected points are being compared with their homologous points identified on the 3D extracted lines. Of course, this set of points is being identified in order to anticipate project and area specificities. According to past commercial projects executed by Terra Spatium, that exploit VHR optical data, an accuracy of 3-4 times the pixel size is being reported.

In the framework of Space for Shore, the cliff lines produced within the Greek test sites, will be validated with in situ GPS measurements during a land survey performed on October 2019.

#### 3.3.4.3 Application Range and Maturity

The maturity of the deployed algorithms is considered high, while in order to achieve a high accuracy, Ground Control Points (GCPs) are needed for the computation of the aerial triangulation. In cases that VHR satellite optical imagery (e.g. Pleiades) is used along with GCPs (measured on the ground) the relative vertical accuracy achieved is around 2meters.

### 3.3.5 Algorithm 3e - Beach width computation

#### 3.3.5.1 Algorithm Description

- *Input data*

This algorithm requires several inputs:

- A reference line that is used to compute the beach width. This reference line can be the foot of the dune, cliff or coastal defence or any other line meaningful to end-users.
- A water line that is used to compute the beach width. This waterline can be extracted from optical or SAR HR/VHR images.
- The tide level at which the end-user wants the beach width to be computed. For instance, some end-users will prefer to know the beach width at high tide to assess the recreative potential of their beach.
- *Algorithms*

Roughly, the beach width is computed as the distance between a reference line denoting the foot of either the dune, or the cliff, or a defence structure and the waterline computed at low tide (total beach width), high tide (upper beach width) or using a time-averaged waterline (mean beach width in microtidal environment). Waterline is detected using algorithm of group 2 (Algorithm Group 2: Waterline and creek edge detection). For instance, along sandy coast experiencing large tidal variation the beach width will correspond to the distance between the dune foot and the waterline at high tide such as shown in Figure 3-24. This distance will be computed along transects perpendicular to the reference line and regularly spaced (10 – 100 m). An alongshore interpolation of the beach width may be required to produce a more continuous data. In area with microtidal environment the middle of swash zone appears as the best proxy of the waterline to compute the mean beach width.

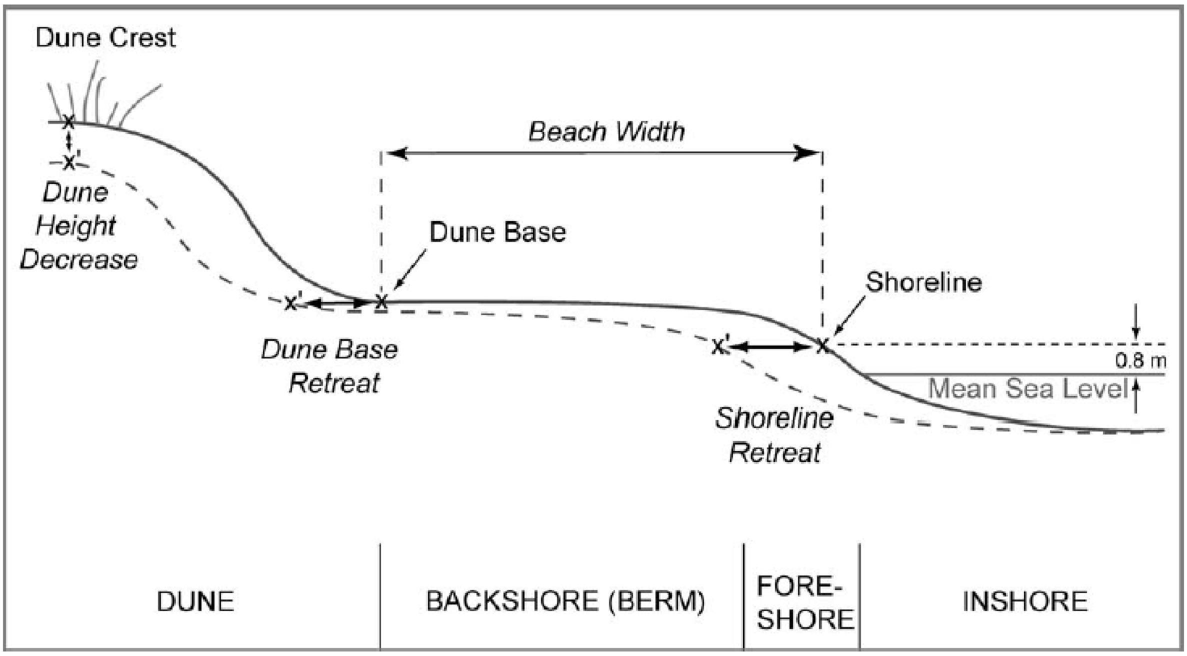


Figure 3-24 - Schematic view of a typical beach elevation profile (cross-shore view) along sandy coasts where the beach width definition is indicated. The 0.8-m water level use to define the shoreline position correspond to the highest water level resulting from tide effect. Extracted from Burroughs and Trebbens (2008).

- *Tools*

Python, QGIS, DSAS

- *Output product*

Shapefile containing the reference line and the corresponding beach width along that line (Figure 3-25).

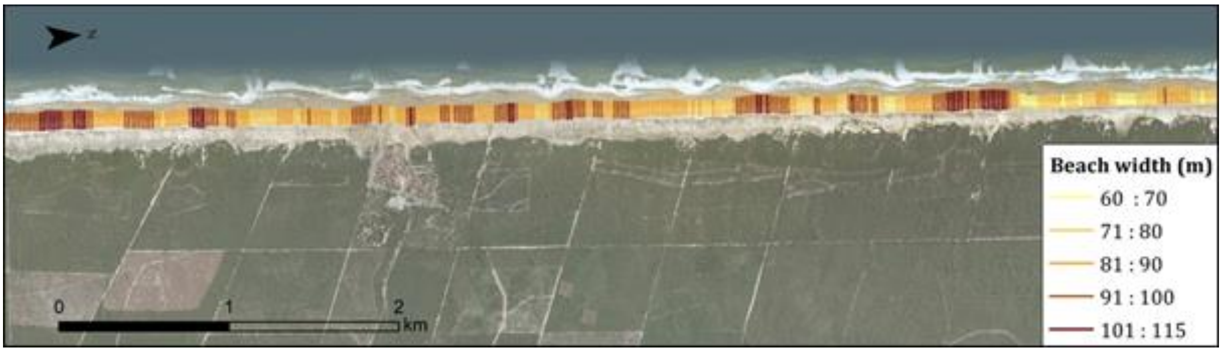


*Figure 3-25 - Example of beach width result*

### 3.3.5.2 Validation

The horizontal accuracy of this algorithm is conditioned by both the accuracy of the waterline and the reference line. In case the reference line is provided by the end-user (no spatial error) and not derived from satellite imagery, the accuracy reduces to the accuracy of the water line extraction algorithm, which usually is of the order of the image pixel resolution (sub-metric to pluri-metric).

### 3.3.5.3 Application Range and Maturity

Although not published, the maturity is high. This algorithm applies to any beaches (e.g. sandy, shingle) as long as the waterline can be extracted from optical of SAR images.

### 3.3.6 Algorithm 3h- Dune foot extraction using supervised classification

#### 3.3.6.1 Algorithm Description

- *Input data*

This algorithm is designed to work with HR multispectral images, although its relevance depends on:

- the average change rates
- the duration of the temporal window addressed.

The slower the dune transition moves and the shorter the temporal window is, the higher the resolution must be. For instance, image resolution of the order of 10 m, such as provided by Sentinel-2 and SPOT4-5, is enough to assess the coastal dune foot retreat during the past 25 year in SW France where the average retreat rates are larger than 0.5-1/yr.

- *Algorithms*

Supervised classification method is applied to distinguish the beach area made of sand from the dune area which is usually covered by vegetation or if not by sand ridge casting shadows around. The most seaward contour of the vegetated dune class is taken as the proxy of the dune. Visual inspection of automatically extracted dune foot lines is necessary to allow manual correction/digitization in case the classifier fails in some regions of the study domain.

- *Tools*

The algorithm uses bash and python programming languages with support of sci-kit learn, Orfeo ToolBox and GDAL libraries. QGIS will be used for visual inspection and digitalization.

- *Output product*

The output of this algorithm is a vector of dune foot positions.

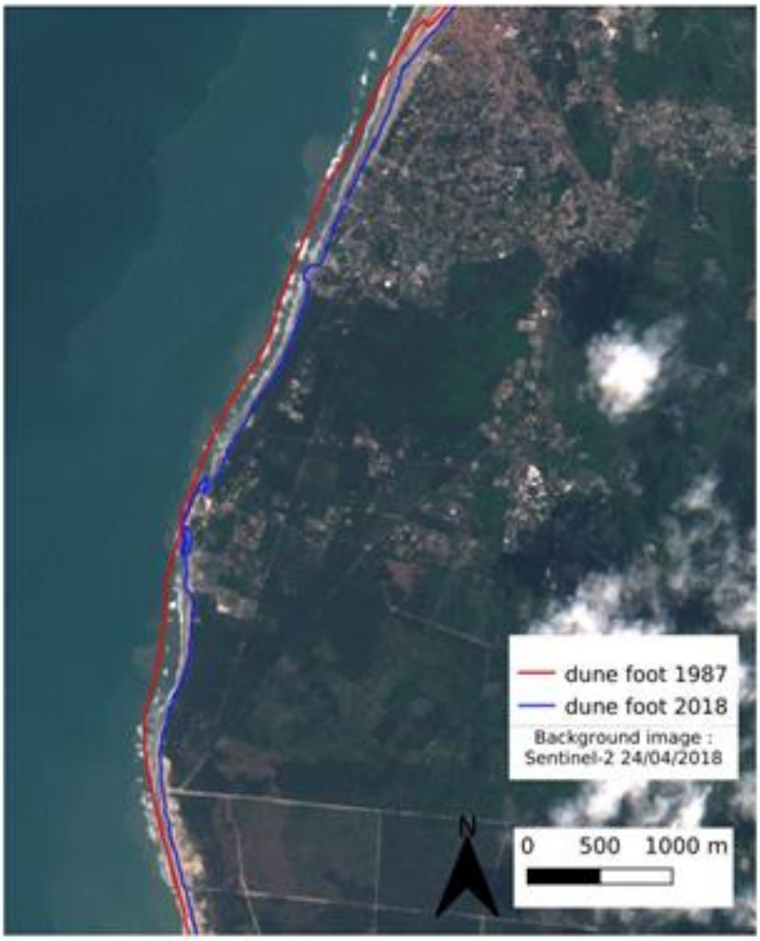


*Figure 3-26 - Dune foot extracted in 1987 and 2018 from Sentinel-2 images*

### 3.3.6.2 Validation

To validate the position of the dune foot in Aquitaine, we use the reference data provided by the Observatory of the Aquitaine Coast (OCA) available in the PYGMA catalog. The available dates are 1998, 2016, 2017 and 2018. On the ArcGIS GIS platform, points are generated every 20 m along the line of the dune foot extracted from satellite images for these four dates. With the "Near" tool, the distance is measured for each date between each point and the nearest in-situ dune foot position. According to Vos *et al*. 2019 subpixel accuracy can be reached for waterline extraction along sandy beaches based on supervised classification. Here, an accuracy of the order of the pixel size is expected as the transition between the dune system and the beach is less clear than for the transition between the water and the beach.

### 3.3.6.3 Application Range and Maturity

This algorithm should provide accurate results only for coastal areas with well-developed dunes covered by vegetation and showing relatively narrow dune face with respect to the image resolution. In case the transitional area between the beach and dune system is wide the extracted interface will correspond more to the dune scarp top line. Also, the comparison of subsequent dune foot lines will only be relevant if addressing temporal period large enough so that the observed changes are larger than the image resolution. While the classification method and diverse regularization methods are used routinely, the reference database for this kind of application need to be built by manually digitizing reference polygons over a subset of images. The algorithm can be considered as mature.

### 3.3.7 Algorithm 3i- Cliff line extraction using supervised classification

#### 3.3.7.1 Algorithm Description

- *Input data*

This algorithm is designed to work with HR multispectral images, although its relevance depends on:

- the average change rates
- the duration of the temporal window addressed. HR SAR data can also be used, specifically for the dune foot detection.

The slower the cliff lines move and the shorter the temporal window is, the higher the resolution must be. For instance, image resolution of the order of 10 m, such as provided by Sentinel-2 and SPOT4-5, can be enough to detect small cliff retreat during the past 25 years at Erretegia cliffs (SW France) where large landslides have occurred or along some cliffs in Normandy (N France) which are particularly dynamic.

According to the geometry and surface typology of the cliff studied and according to which lines (cliff top and/or cliff foot), the images used in the supervised classification must:

- contain particular spectral features; and/or
- be acquired at particular tide level and/or
- be acquired with particular viewing angle and sun elevation.

For instance, the presence of shadows seaward the cliff top can help detecting the cliff top, while it may prevent form detecting the cliff foot. The presence of a ground cover landward the cliff top with spectral signature very different from what can be observed on the cliff face and seaward is also crucial. Also, the use of images only acquired at high tide may allow detecting the cliff base at some sites where the cliff face is steep and when the satellite field of view is not obstructed by the cliff top.

- *Algorithms*

Regardless of the type of cliff line to be detected, a supervised classification method is applied to discriminate the different classes of ground cover, the main ones being:

- water; wet/dry
- sand/shingle beach
- rock
- terrestrial
- vegetation
- urbanization
- mix of vegetation
- Urbanization
- shadow.

Then, distinct strategies are used for the extraction of cliff foot and cliff top. These extraction strategies are site-specific and can be fully described/implemented only once a minimal knowledge about the site is reached and following an analysis of the image dataset to identify what are the features consistently present in the images.

**Cliff top:** Usually the cliff top line will be located by the boundary between the classes: terrestrial vegetation; urbanization; mix of vegetation, and the other classes located seaward the cliff top such as the classes of: water, wet/dry sand/shingle, rock. The combination of steep cliff faces oriented in a direction opposite to the sun position, low sun elevation will cause shadows to appear. In that case, the cliff top line is easily located by the boundary between the classes: terrestrial vegetation; urbanization; mix of vegetation, and the class: shadow.

**Cliff foot:** For cliff suffering erosion mainly from wave attacks, it can be reasonably assumed that during highest tide level the water domain will be in direct contact with cliff, without presence of beach or low-slopping rocky platforms in between. In case the geometrical conditions of the cliff regarding the sun exposition ensure that no any shadow is projected down the cliff, a relevant proxy for the cliff foot is the waterline at high tide. However, the tide level at high tide varies from one date to another due to varying tide cycle and the presence of wave set-up and storm surge. Unless the cliff is a vertical wall, these variations lead to meter-scale horizontal shifts of the waterline along the cliff face. The use of the latter proxy is then relevant only for steep cliffs and for addressing long-term changes, which both make the errors introduced by the latter reasoning negligible.

A necessary condition for cliff line extraction is the use of images acquired with a low viewing angle. The closer to the nadir the image is acquired the more accurate will be the positioning of the cliff lines. Basically, even after image georeferencing, a sensor located over the water domain imaging the cliff face will tend to put the pixels of cliff top too much landward. The opposite phenomenon occurs for a sensor located over the land domain with a tendency to shift seaward the top of the cliff. For this latter mode of acquisition, the cliff foot may also not be seen by the sensor when the cliff face is steep enough.

A narrow buffer area along the cliff (indicating where the cliff lines are expected to be found) has to delimited to drive the identification of the inter-class boundaries corresponding to the cliff lines. Finally, a visual inspection of automatically extracted cliff lines is necessary to allow manual correction/digitization in case the classifier fails in some regions of the study domain.

- *Tools*

The algorithm uses bash and python programming languages with support of sci-kit learn, Orfeo ToolBox and GDAL libraries. QGIS will be used for visual inspection and digitalization.

- *Output product*

The output of this algorithm is a vector of cliff foot and/or cliff top positions.

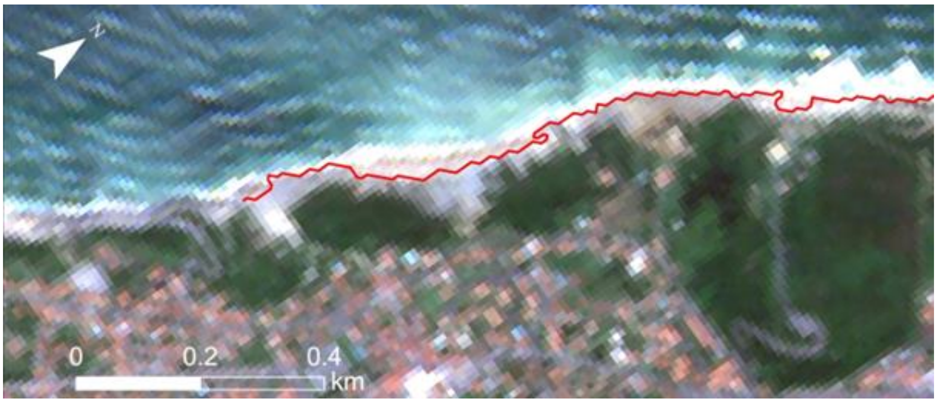


*Figure 3-27 - Cliff foot extracted from Sentinel-2 images*

### 3.3.7.2 Validation

The cliff lines are validated from cliff lines extracted from very high-resolution DEM (LiDAR), with centimeter precision. The lines of equal slopes are extracted every 10°. The isolines are also extracted each 1 m. The combination of these two information makes it possible to precisely identify the slope discontinuity at high altitude (cliff apex) and the equivalent at low altitude (cliff foot). On the ArcGIS GIS platform, points are generated every 20 m along the cliff apex extracted from satellite images. With the "Near" tool, the distance is measured for each date between each point and the nearest in-situ cliff apex for the same date. This process is also performed for the cliff foot. Considering the numerous potential sources of errors and misinterpretations a maximal accuracy of the order of the pixel size is expected.

### 3.3.7.3 Application Range and Maturity

As discussed previously in this section, this algorithm may not be applicable to all cliffs and designed of the algorithm is mostly site-specific. Also, the comparison of subsequent cliff lines will only be relevant if addressing temporal period large enough or if the changes are brutal (landslides) so that the observed changes are larger than the image resolution. While the classification method and diverse regularization methods are used routinely, the reference database for this kind of application need to be built by manually digitizing reference polygons over a subset of images. Additionally, the automated extraction of the boundaries between several type of class will require significant developments. The maturity of this algorithm can then be considered as almost mature.

## 3.3.8 Algorithm 3j - Top of the cliff movement monitoring using PS with ERS and ENVISAT data

### 3.3.8.1 Algorithm Description

The PS-InSAR technique allowed to perform a pre- and a post-event displacement analysis on the general rock massif stability, evaluating the state of activity of long-term ground displacements.

- *Input Data*

This algorithm has been tested for ERS1/2, ENVISAT SLC data.

- *Algorithms*

For the current application the proper algorithm was selected. Its selection was mainly based on the limited number of available ERS and ENVISAT SAR scenes for the area of study during the examined period. The interferometric possible approach used in this case (ERS 1 & 2 and ENVISAT), collecting a dataset with low temporal and spatial baseline applying the GAMMA/IPTA s/w is summarized in the following steps after coregistration of the scenes:

Multi-reference processing in order to determine point height corrections (using one dimensional regression) as well as unwrapped phases. The unwrapped phases are then converted to a single reference time series using the Singular Value Decomposition (SVD) algorithm.

An alternative possible version that is similar to the previous one is always starting with multi reference processing (more interferometric pairs) and then one reference image stack processing to record the surface deformation.

Following the above technique starting with multi-reference processing we get a larger number of interferometric pairs also we can reduce the longest time interval between acquisitions.

The results achieved are the point height corrections plus the annual average deformation rates in LOS (along the Line Of Sight), time series.

- *Tools*

For this algorithm is going to be used GAMMA/ IPTA.

- *Outputs Products*

As output this algorithm provides deformation maps in LOS (Line of Sight) of satellite.

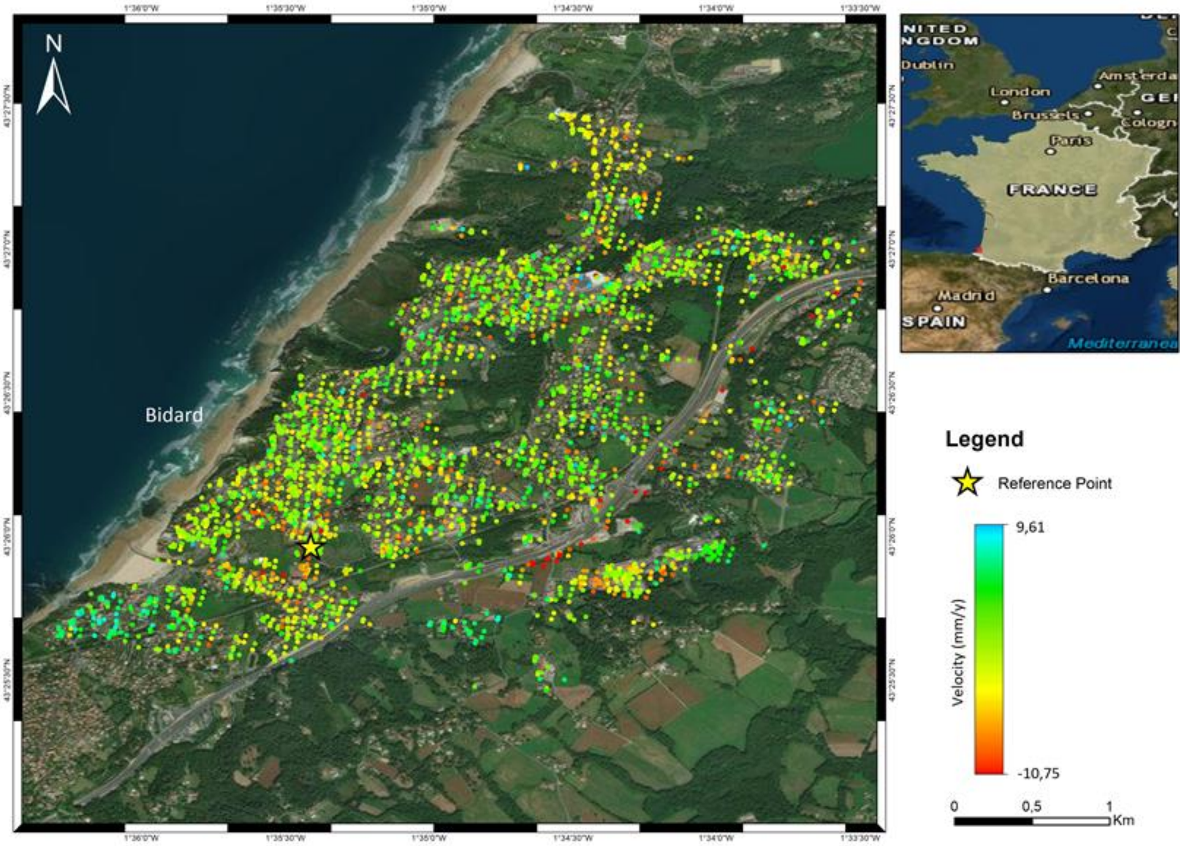


*Figure 3-28 - Example of PSI technique with Sentinel 1 data*

### 3.3.8.2 Validation

For the validation of ground motion many scientists use a monitoring system based on remote sensing techniques, such as radar interferometry ground-based and terrestrial laser scanning, in order to monitor the ground deformation of the investigated area and to evaluate the residual risk (Frodella *et al.,* 2016). More specific for the top of the cliff movement validation Martino *et al.,* 2014 use field-based geomechanical investigations and remote geostructural investigations via a terrestrial laser scanner (TLS). Moreover, Crosetto *et al.,* 2011 using as a validation method for the PSI 2D displacement information (in range and azimuth) using images from a single radar instrument.

### 3.3.8.3 Application Range and Maturity

PSI is an opportunistic deformation measurement method, i.e. it is able to measure deformation only over the available PSs. The PS density is usually low in vegetated, forested and low-reflectivity areas (e.g. very smooth surfaces), and in steep terrains facing the radar sensors. The potential of the PSI technique has been recognized since it was first proposed (Ferretti *et al.*, 2001). In the last fifteen years, a wide range of PSI applications has been developed. At this point we are using a well-tested algorithm who provides very promising results.

## 3.3.9 References

Adolph W., Schückel U., Soo Son C., Jung R., Bartholomä A., Ehlers M., Kröncke I., Lehner S., Farke H., 2017. Monitoring spatiotemporal trends in intertidal bedforms of the German Wadden Sea in 2009–2015 with TerraSAR-X, including links with sediments and benthic macrofauna.- Geo-Marine Letters, April 2017, Volume 37, Issue 2, pp 79–91

Rahmayudi A., Rizaldy A., COMPARISON OF SEMI AUTOMATIC DTM FROM IMAGE MATCHING WITH DTM FROM LIDAR, The International Archives of the Photogrammetry, Remote Sensing and Spatial Information Sciences, Volume XLI-B3, 2016 XXIII ISPRS Congress, 12–19 July 2016, Prague, Czech Republic

Almeida L.P., Almar R., Bergsma E., Berthier E. Baptista P., Garel E., Dada O., Alves B, 2019. Deriving High Spatial-Resolution Coastal Topography From Sub-meter Satellite Stereo Imagery, Remote Sensing, 11(5), 590, doi:10.3390/rs11050590

Letortu P., Jaud M., Théry C., Nabucet J., Passot S., Augereau E., 2019. The potential of Pleiades images with high angle of incidence for reconstructing the Norman coastal cliff face, International Journal of Applied Earth Observations and Geoinformation, submitted

Anys H., Bannari D., He C., Morin D. "Texture analysis for the mapping of urban areas using airborne MEIS-II images." Proceedings of the First International Airborne Remote Sensing Conference and Exhibition 3 (1994): 231-245

Baltsavias E., Pateraki M., Zhang L., 2001. Radiometric and Geometric Evaluation of IKONOS Geo Images and their use for 3D building modelling. Proc. Joint ISPRS Workshop "High Resolution Mapping from Space 2001", Hannover, Germany, 19-21 September

Eisenbeiss H, Baltsavias E, Pateraki M., Zhang L., 2004. Potential of IKONOS and QuickBird imagery for accurate 3D point positioning, orthoimage and DSM generation. International Archives of the Photogrammetry, Remote Sensing and Spatial Information Sciences. 35

Battiau-Queney Y., Billet J.F., Chaverot S., Lanoy-Ratel P., 2003. Recent shoreline mobility and geomorphologic evolution of macrotidal sandy beaches in the north of France, Marine Geology, 194, pp. 31-45, doi: S0025-3227(02)00697-7

Berardino P., Fornaro G., Lanari R., Sansosti E., 2002. A new algorithm for surface deformation monitoring based on small baseline differential SAR interferograms. IEEE Transactions on Geoscience and Remote Sensing, 40 (11), 2375-2383

Boak E.H., Turner I.L., 2005. Shoreline definition and detection: A review. Journal of Coastal Research, 21(4), 688–703. doi:10.2112/ 03-0071.1

Briese C., 2004. Three-Dimensional Modelling of Breaklines from Airborne Laser Scanner Data. In International Archives of Photogrammetry and Remote Sensing, Vol. XXXV, B3, Istanbul, Turkey, pp. 1097 – 1102

Brzank A., Lohmann P., Heipke C., 2005. Automated extraction of pairwise structure lines using airborne laser scanner data in coastal areas, International Archives of Photogrammetry and Remote Sensing, ISPRS Workshop Laser Scanning 2005, Enschede, Netherlands, 36, Part 3/W19, pp. 36–41

Burroughs S.M., Tebbens S.F., 2008. Dune Retreat and Shoreline Change on the Outer Banks of North Carolina, Journal of Coastal Research, 24(2b), 104–111, doi:10.2112/05-0583.1

Castelle B., Marieu V., Bujan S., Splinter K.D., Robinet A., Sénéchal N., Ferreira S., 2015. Impact of the winter 2013–2014 series of severeWestern Europe storms on a double-barred sandy coast: Beach and dune erosion and megacusp embayments, Geomorphology, 238, p. 135-148, doi:10.1016/j.geomorph.2015.03.006

Crosetto M., Monserrat O., Cuevas-González M., Devanthéry N., Crippa B., 2011. Analysis of X-band very high resolution Persistent Scatterer Interferometry data over urban area. International Archives of the Photogrammetry, Remote Sensing and Spatial Information Science, Hannover, Germany, 21-24

Ferretti A., Prati C., Rocca F., 2000. Nonlinear subsidence rate estimation using permanent scatterers in differential SAR interferometry. IEEE Transactions on Geoscience and Remote Sensing, 38 (5), 2202–2212

Ferretti A., Prati C., Rocca F., 2001. Permanent scatterers in SAR interferometry. IEEE Transactions on Geoscience and Remote Sensing, 39 (1), 8-20

Frodella W., Ciampalini A., Gigli G., Lombardi L., Raspini F., Nocentini M., Scardigli C., Casagli N., 2016. Synergic use of satellite and ground based remote sensing methods for monitoring the San Leo rock cliff (Northern Italy), Geomorphology, 264, pp. 80-94

Gade M., Melchionna S., 2016. Jint Use of Multiple Synthetic Aperture Radar Imagery for the Detection of Bivalve Beds and Morphological Changes on Intertidal Flats, Estuar. Coast. Shelf Sci., 171, 1-10, doi:10.1016/j.ecss.2016.01.025

Gomes Pereira L.M.G., Wicherson R.J., 1999. Suitability of laser data for deriving geographical information: a case study in the context of management of fluvial zones. ISPRS Journal of Photogrammetry and Remote Sensing 54(2–3): 104–114

Grodecki J., Dial G., 2003. Block Adjustment of High-Resolution Satellite Images Described by Rational Polynomials. Photogrammetric Engineering & Remote Sensing, 69(1): 59-68

Gruen A., 1985, Adaptive Least Squares Correlation: A powerful Image Matching Technique. South Africa Journal of Photogrammetry, Remote Sensing and Cartography, 14 (3), pp. 175-187

Gruen A., Zhang L., 2004. Automatic DSM generation from linear array imagery data. Int. Archives of the Photogrammetry, Remote Sensing and Spatial Information Sciences, Istanbul, Turkey, Vol XXXV, Part B3, pp. 128-133

Guillén J., Stive M.J.F., Capobianco M., 1999. Shoreline evolution of the Holland coast on a decadal scale. Earth Surf. Process. Landforms, 24, p. 517-536

Hanley H.B., Yamakawa T., Fraser C.S., 2002. Sensor Orientation for High-Resolution Satellite Imagery. International Archives of Photogrammetry & Remote Sensing, 34(1): 69-75

Hapke C.J., Reid D., 2007. National Assessment of shoreline change, Part 4: Historical coastal cliff retreat along the California coast. USGS Open-File Report 2007–1133, 51p

Hoeke R.K., Zarillo G.A., Synder M., 2001. A GIS based tool for extracting shoreline positions from aerial imagery (Beach-Tools), Proceedings of ERDC/CHL CHETN-IV-37

Lafon V., Hoareau A., Mallet C., Desprats J.F., 2010. Suivi du trait de côte en Aquitaine par imagerie Formosat-2. Actes des 10ièmes JNGCGC, Sables D’Olonne, vol. 2, p. 497-504

Lafon V., Dehouck A., Robinet A., Marieu V., Curti C., Durou N., 2014. Détection d’indicateurs géomorphologiques littoraux par télédétection à très haute résolution spatiale (pp. 601-610), doi:10.5150/jngcgc.2014.066

Laporte-Fauret Q., Marieu V., Castelle B., Michalet R., Bujan S., Rosebery D., 2019. Low-Cost UAV for High-Resolution and Large-Scale Coastal Dune Change Monitoring Using Photogrammetry, Journal of Marine Science and Engineering, 7(3), 63, doi: 10.3390/jmse7030063

Le Mauff B., Juigner M., Ba A., Robina M., Launeaub P., Fattal P., 2018. Coastal monitoring solutions of the geomorphological response of beach-dune systems using multi-temporal LiDAR datasets (Vendée coast, France), Geomorphology 304, P., 121–140, doi: 10.1016/j.geomorph.2017.12.037

Lemaire C., 2008. Aspects of the DSM production with high resolution images. International Archives of the Photogrammetry, Remote Sensing and Spatial Information Sciences, Vol.XXXVII, Part B4, pp.1143-1146

Li Z., Gruen A., 2004. Automatic DSM generation from linear array imagery data. Int. Archives of the Photogrammetry, Remote Sensing and Spatial Information Sciences, Istanbul, Turkey, Vol XXXV, Part B3, pp. 128-133

Liu J.K., Li R., Deshpande S., Niu X., Shih T.Y., 2009. Estimation of Blufflines Using Topographic Lidar Data and Orthoimages, Photogrammetric Engineering & Remote Sensing, 75, pp. 69–79

Martino S., Mazzanti P., 2014. Integrating geomechanical surveys and remote sensing for sea cliff slope stability analysis: The Mt. Pucci case study (Italy)

Massonnet D., Rabaute, T., 1993. Radar interferometry: limits and potential. IEEE Trans. Geosci. Remote Sensing 31, 455–464

Nahon A., Molina P., Blázquez M., Simeon J., Capo S., Ferrero C., 2019. Corridor Mapping of Sandy Coastal Foredunes with UAS Photogrammetry and Mobile Laser Scanning, Remote Sensing, 11(1352), doi:10.3390/rs11111352

O'Dea A., Brodie K. L., Hartzell P., 2019. Continuous Coastal Monitoring with an Automated Terrestrial Lidar Scanner, Journal of Marine Science and Engineering, 7, 37, doi:10.3390/jmse7020037

Palaseanu-Lovejoy M., Danielson J., Thatcher C., Foxgrover A., Barnard P., Brock J., Young A., 2016. Automatic Delineation of Seacliff Limits using Lidar-derived High-resolution DEMs in Southern California, Journal of Coastal Research, 26, 162–173

Toure S., Diop O., Kpalma K., Maiga A.S., 2019. Shoreline Detection using Optical Remote Sensing: A Review, International Journal of Geo-Information, 8, 75, doi:10.3390/ijgi8020075

Reinartz P., D ' Angelo P., Krauß T., Chaabouni-Chouayakh H., 2010. DSM Generation and Filtering from High Resolution Optical Stereo Satellite Data, Remote Sensing for Science, Education, Natural and Cultural Heritage, EARSeL, 2010

Richter A., Faust D., Maas H.G., 2013. Dune cliff erosion and beach width change at the northern and southern spits of Sylt detected with multi-temporal Lidar, Catena, 103, p. 103-111, doi:10.1016/j.catena.2011.02.007

Robertson W., Zhang K., Whitman D., 2007. Hurricane-induced beach change derived from airborne laser measurements near Panama City, Florida. Marine Geology, 237, p. 191–205, doi:10.1016/j.margeo.2006.11.003

Roche A., Bosc C., Chandelier L., Lagnous R., 2014. Apport de l'imagerie satellitaire pour le suivi du trait de côte. XIIèmes Journées Nationales Génie Côtier – Génie Civil Dunkerque, 2-4 juillet 2014, doi:10.5150/jngcgc.2014.068

Santel F.,Linder W., Heipke C, 2004. Stereoscopic 3D-image sequence analysis of sea surfaces. In ISPRS Commission V Symposium, Vol. 35, pp. 708–712

Tao V., Hu y., 2002. 3D Reconstruction Methods Based on the Rational Function Model. American Society for Photogrammetry and Remote Sensing. 68,705-714

Vos K., Splinter K.D., Harley M.D., Simmons J.A., Turner I.L., 2019. CoastSat: a Google Earth Engine-enabled Python toolkit to extract shorelines from publicly available satellite imagery. Environmental Modelling and Software. 122, 104528

Zarillo G.A., Kelley J., Larson V., 2008. A GIS Based Tool for Extracting Shoreline Positions from Aerial Imagery (BeachTools) Revised, Proceedings of ERDC/CHL CHETN-IV-73

## 3.4 ALGORITHM GROUP 4: BATHYMETRY

### 3.4.1 Introduction

The knowledge about nearshore bathymetry is of paramount importance to oceanography research, management and economic activities. Nevertheless, bathymetric data acquisition in shallow waters (0 to 50 m) with traditional methods (e.g., single and multi-beam echo sounder) have disadvantages such as safety and cost. For these reasons, satellite remote sensing has become increasingly important in the bathymetry estimation. Some works have delved into swell properties in the nearshore area due to the interaction with the sea-bottom to infer the bathymetry (e.g., Brusch et al., 2011; Mishra et al., 2014; Pereira et al., 2019) (Figure 3-29). Other works focused on the use optical satellite sensors to retrieve bathymetry either by:

- calibrating an empirical model with in situ survey data (e.g. Lyzenga *et al.,* 2006) or
- calibrating a radiative transfer model which decomposes the radiometric intensity recorded at the water surface into contributions from the water column and the water bottom (Lee *et al.,* 2002; Capo *et al.,* 2014, Dekker *et al.,* 2011).

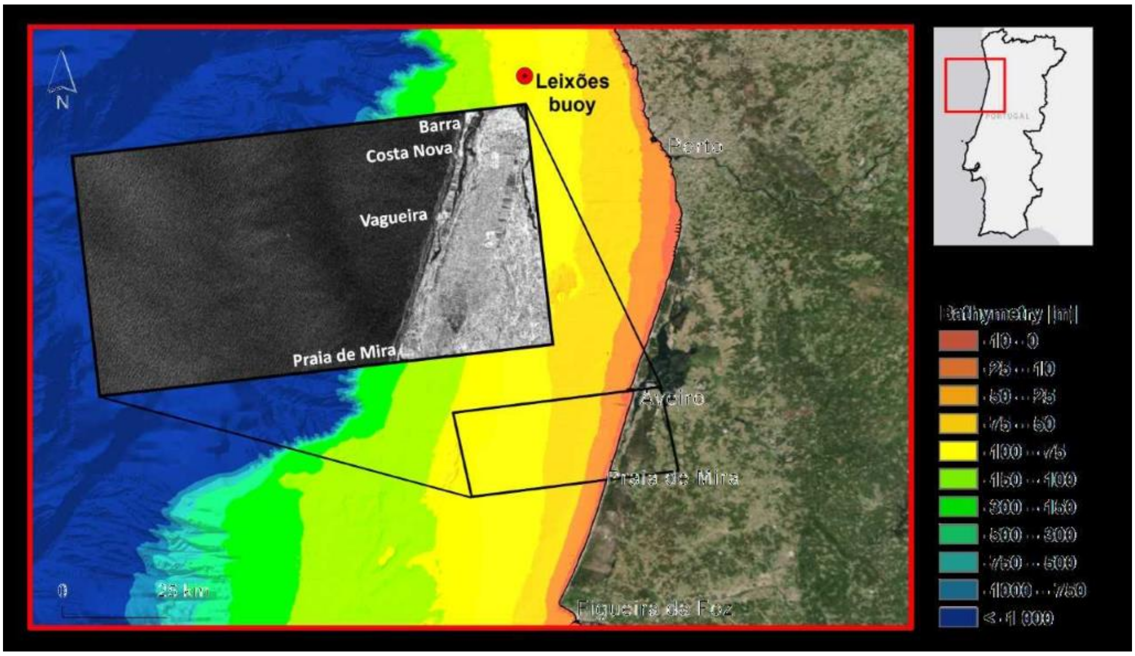


Figure 3-29 - Bathymetry map with the location of the Leixões buoy and the Sentinel-1A sub-image (black rectangle) between Barra and Praia de Mira (W Portugal) (modified from Pereira et al., 2019).

### 3.4.2 State-of-the-art

Several remote sensing techniques have been proposed to estimate the water depth in the last decades. In the case of optical sensors, there are two main approaches. In the first, available in situ data is used to calibrate parameters of an empirical model (Lyzenga *et al.,* 2006; Stumpf *et al.,* 2003) in which each water penetrating spectral band of the optical sensor is used in a linear combination. In the second type of approaches, a radiative transfer model is calibrated by estimating inherent and apparent optical properties of the water column by jointly exploiting water penetrating spectral bands of the sensor. Classical high resolution optical sensors (SPOT-5-6-7, Pleiades, Sentinel-2, Landsat-8, etc.) only offer a few water colour sensitive spectral bands and the radiative transfer model is simplified by considering some water optical properties as constant in the image (for instance bottom albedo and attenuation coefficients) and by empirically calibrating other parameters (for instance water absorption and backscattering). This has led to the development of a Quasi Analytical Algorithm (QAA) to resolve this calibration using water surface reflectance as inputs and water depth as an output (Lee *et al.,* 2002; Capo *et al.,* 2014). For hyperspectral sensors alternative approach to resolve radiative transfer model equations exists (e.g. Dekker *et al.,* 2011), which are more adapted to very heterogeneous bottom conditions. Nevertheless, the utilization of such approach is limited by the water transparency and the variability in the optical properties of the water column and the reflecting bottom material (Adler-Golden *et al.,* 2005). Therefore, its application in high energetic coasts with suspended sediments is restricted to water depths from 0 to 6 m. This limitation motivated the development of alternative methods which are focused on the change of wave properties due to the interaction with sea bottom topography (Brusch *et al.,* 2011). When the waves propagate from deeper to shallower water their wavelength decreases and their direction changes, and as a result these properties allow to infer sea bottom features. Brusch *et al.* 2011 proposed for the first time, the application of the Fast Fourier Transform (FFT) over Synthetic-Aperture Radar (SAR) image to obtain a directional spectrum and then, to calculate the wavelength and wave direction and to estimate the water depth. These authors worked with SAR data obtained from the commercially available TerraSAR-X (TSX) data. After that, other authors have applied this methodology to SAR data obtained from the RISAT-1 commercial products (Mishra *et al.,* 2014) and Sentinel-1 missions (Wiehle and Pleskachecsky, 2018; Pereira *et al.,* 2019). Pereira *et al.* 2019 compared the computed with the measured bathymetry to Aveiro coast (W Portugal) and they found the relative error of the water depth varies from 6% to 10%. Alternatively, to the Fast Fourier Transform (FFT), the Wavelet transform (Chui, 1992) is more adequate to represent non-linear wave processes more common in shallow waters and can be used instead to the FFT in this nearshore domain (Abreu *et al*., submitted).

## 3.4.3 Algorithm 4b - Quasi-analytical model to retrieve bathymetry from HR/VHR optical data

### 3.4.3.1 Algorithm Description

- *Input data*

Five main input data are needed to perform this approach:

- Water surface reflectance image (mainly the green band) obtained after performing three pre-processing steps consisting in (1) atmospheric correction, (2) mask of non-water pixels, (3) sun glint correction
- Deep water mask used to calibrate deep water parameters of the model
- Pre-calibrated parameters of the QAA algorithm empirically estimated using IOP / AOP databases[1] and spectral sensitivity of the targeted optical sensor
- Bottom types map and bottom albedo if the targeted sites display heterogeneities
- Tide level at time of image acquisition to transform water depth into water level in accordance to the hydrographic reference level

- *Algorithms*

The application of the QAA algorithm follows a four-steps strategy as described in Capo *et al.* 2014:

- The deep-water mask defined during the pre-processing steps is used to estimate the mean deep water subsurface remote sensing reflectance ($r_{rs}^{deep}$) for the targeted spectral band. The bottom albedo ($R_{rs}^{B}$) is considered as known but if the bottom type is homogeneous (sandy shore for instance), automatic strategies exist to directly infer the albedo from the image.
- From $r_{rs}^{deep}$, the total absorption and backscattering are estimated followed by the attenuation coefficient $K_d$ in accordance with the equations of the QAA (Lee *et al.,* 2002).
- Then, the water depth $h$ is estimated using the following equation:
- Finally, water depths are converted into bathymetric values using the tide level at the time of image acquisition.

- *Tools*

As previously, two main software and toolboxes are needed essentially for the pre-processing steps:

- ACOLITE software for atmospheric correction of Sentinel-2, Landsat-8 and recently Pleiades data
- OTB toolbox for atmospheric correction of other optical sensor and to perform the supervised classification and mask generation

- *Output product*

The output product is directly a raster file containing bathymetry estimation for each valid water pixels. It can be converted to a xyz file or to iso-contours if requested.

### 3.4.3.2 Validation

The accuracy is generally poorer than with the empirical approach and RMSE reaches 1.3 m in the study of Capo et al. 2014. Figure 3-30 shows a satellite derived bathymetry produced by i-Sea with image acquired in 2015 on the French Mediterranean coastline using a Pleiades data along with comparison with observations from a LIDAR survey. Results revealed a RMSE of 0,6 m on the entire area and an overall accurate detection of the nearshore sandbar location.

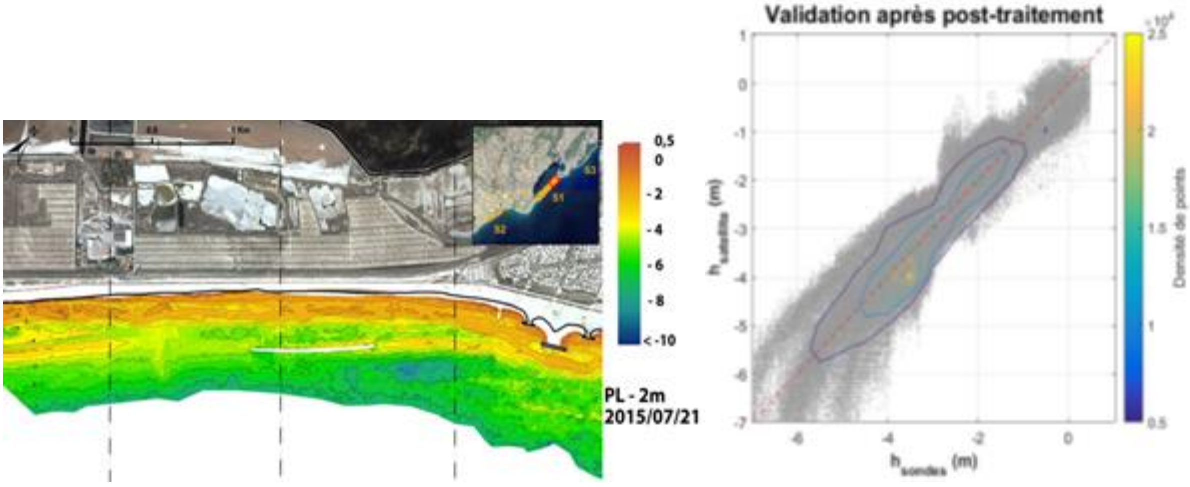


Figure 3-30 - *Example of optical satellite derived bathymetry at the Lido de Sète (S France) with a Pléiades image acquired in 2015 and validation results.*

### 3.4.3.3 Application Range and Maturity

This QAA approach can retrieve reliable depth up to 10 to 15 m in clear waters with bright sandy substrate. For example, in Capo *et al.* 2014 study on the French Atlantic sandy coastline, depths of up to 7 m have been retrieved successfully. Similar to the above-mentioned empirical approach, a few drawbacks have to be noted. It also assumes constant water conditions across the area and it is sensitive to bottom heterogeneity. The presence of clouds, shadows and waves can also restrict the method application. Also, because water depths need to be corrected from the tide level, data from tide modes or tide gauges.

Nevertheless, this approach is cost effective and does not require *in situ* data, which are often missing or outdated in many places worldwide. Its maturity can be considered as high.

## 3.4.4 Algorithm 4c (i,ii) - Bathymetry swell inversion

### 3.4.4.1 Algorithm Description

- Input Data

The Optical/SAR georeferenced images in which swell condition are present (*i.e.*, the wave period of the images must be higher than 15 seconds).

The wave data from a directional wave buoy or from ERA5 dataset for the date of image acquisition are recommended to estimate the offshore wavelength. Nevertheless, if wave data are not available wavelength can be computed from the satellite image.

The astronomical tidal level for the date of image acquisition is required.

- Algorithms

There are two bathymetry swell inversion algorithms according to the spectral analysis used:

1. The algorithm 4ci-Fast Fourier Transform (FFT) that is suitable to estimate bathymetry to depth waters (z=15 – 30 m). This approach follows a four-steps procedure as described by Pereira *et al.* 2019 and Stelzer *et al.* 2019:

   The first step consists in the definition of a grid of centre points over the image. These points define the positions in the image where the local (*i.e.,* in the vicinity of each point) estimation of the wave characteristics (*i.e.* wave direction and wavelength) is performed. Next, a squared region (image cell) centred in each point of the grid is defined, whose width is specified independently of the grid spacing (in this way, partial superposition between adjacent cells is allowed).

The second step is the spectral analysis for each defined squared cell resulting in a two-dimensional frequency-domain representation of the information content of each cell in the image. The FFT represents the energy that a signal shows distributed with respect to the frequency of each of its components, when considering a decomposition of such signal in sinusoidal components. If a signal displays a sinusoidal-like dominant component, this Fourier representation will reveal a high peak of energy at the frequency of such component. Thus, it will be a suitable tool for estimating the characteristics of the dominant sea waves (i.e. wavelength and wave direction) in a specific region. The wavelength (λ) (in number of pixels) of the dominant surface wave of that cell can be estimated through (Eq.1):

$$\lambda = \frac{1}{\left(\frac{dx}{2M}\right)2} + \left(\frac{dy}{2N}\right)2$$

where *M* is the number of columns of pixels, *N* is the number of rows of pixels, *dx* is the number of columns between two identified peaks in the frequency-domain representation of the cell image and *dy* the respective difference in number of rows.

The value of the wavelength in meters is then obtained from the former by considering the image spatial resolution. The wave direction is the orientation of the segment connecting the two identified sharp peaks.

The wavelengths and wave directions are associated to the coordinates of the centre point of the corresponding cell, in the georeferenced coordinate system provided by the coordinated control points which are attached to the satellite image.

The third step is the bathymetric estimation from linear wave theory also known as Airy theory. This is an analytical solution of the momentum and mass conservation equations that describe the velocity field and pressure along the water column and establishes a relation between the wave celerity, the frequency and the water depth (linear dispersion relation).

The approach considered for determining the sea-bottom depth (h) satisfies the set of values of the wavelength (λ) and the wavelength at deep water ($\lambda_0$) given in the linear dispersion relation:

$$\lambda = \lambda 0 \tanh\,(kh)$$

where $\lambda_0=gT^2/2\pi$, T is the wave period, g is the gravity acceleration, k is the wave number and h is the sea-bottom depth. The effect of a mean current was neglected.

The bathymetry is computed from:

$$h = 2\,\mathrm{atanh}\left(\frac{\lambda}{\lambda 0}\right)$$

The last step is the application of low-pass filter to remove the noise in the computed values. This filter has two input parameters: the filter width is the scalar indicative of the width of the filter and the filter sharpness is the scalar indicating how sharp the transition between the pass- and reject-bands is.

2. The algorithm 4cii- Wavelet Transform (WT) that is suitable to estimate bathymetry to shallow waters (z= 1 – 15 m). This approach follows a three-steps procedure as described by Abreu *et al.* 2017, 2019:

   The first step consists in converting the image in a matrix where each value of the matrix corresponds to the intensity of the pixel grey shade.

   The second step is the spectral analysis with WT along each row and column of the matrix in order to estimate the wave characteristics (*i.e.* wavelength). Since the processed signal is obtained from the matrix reading through rows and columns, the methodology applied provides the horizontal and vertical components of the wavelength ($\lambda_x$ and $\lambda_y$). Thus, the wavelength λ can be computed from the knowledge of both components as:

$$\lambda = \lambda\chi * \frac{\lambda y}{\sqrt{\lambda\chi^2 + \lambda y^2}}$$

The third step is the bathymetric estimation from linear wave theory also known as Airy theory as was described for FFT.

- Tools

A set of Matlab routines were implemented to address both approaches.

- Outputs Products

The output product is directly a file containing bathymetry estimation for the domain covered by the linear dispersion relation. The output can be presented in a xyz file. Additionally, a bathymetry map can be created using a kriging interpolation in GIS software upon request.

### 3.4.4.2 Validation

The satellite derived bathymetry using the swell inversion algorithm 4ci-FFT for Portuguese coast was compared with the bathymetry provided by the Oceanographic Observatory of the Iberian Margin (RAIA Observatory). The results disclosed that 20 m estimated isobaths provided the best performance whereas the 35 m estimated isobaths provided the lowest performance (Figure 3-31). The relative error of the water depth varies between 6% and 10% (Pereira et al., 2019).

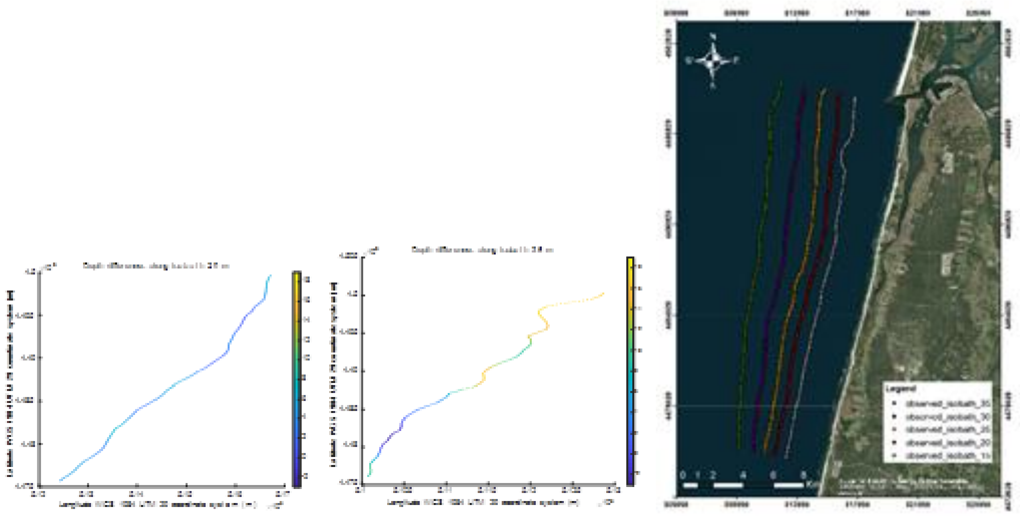

Figure 3-31 - *Depth differences in meters between observed isobaths (20 and 35 m) and satellite derived depths at these locations at Aveiro coast (Portugal).*

The satellite derived bathymetry using the swell inversion algorithm 4cii-WT has not been validated yet.

### 3.4.4.3 Application Range and Maturity

The algorithm 4ci-FFT, which is adequate for water depths between 15 m and 30 m, has been tested at Aveiro coast (Portugal) in images of different years: 2011, 2015 and 2019 (Pereira *et al.,* 2019; Fernández *et al.,* 2020) and at Bidart and Erretegia coast (France) in an image of year 2018 (Fernández *et al.,* 2020). This algorithm can be considered as a demonstration algorithm only tested in two test sites with a set of seven images. The results obtained show that the relative error of the water depth ranges between 6% and 10% for water depths between 15 and 30 m.

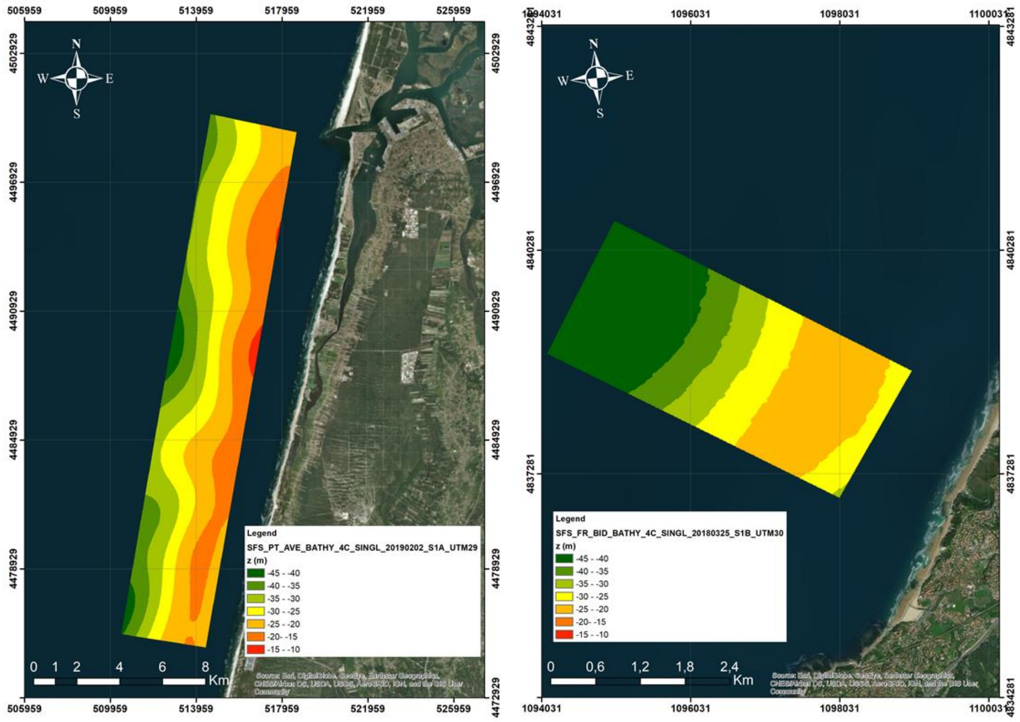


Figure 3-32 - *Satellite derived bathymetry using swell inversion algorithm with FFT for: a) Aveiro coast (Portugal) in February 2019 and b) Bidart coast (France) in March 2018.*

The algorithm 4cii- WT, which has been developed for water depths between 1 m and 15 m, has been only tested in a section of one satellite image at Aveiro coast (Portugal). The obtained results allow only infer that it is adequate to estimate the sea-bottom morphology but the accuracy assessment has not been already performed. It can be considered as an innovative or experimental algorithm.

### 3.4.5 References

Abreu T., Fernández-Fernández S., Baptista P., Silva P.A., 2020. Utilização de wavelets para inferir a batimetria a partir de imagens de satélite SAR. In: VIII Tomo da Rede BRASPOR: Saindo da Zona de Conforto: a Interdisciplinaridade das Zonas Costeiras

Abreu T., Matos J., Pereira P., Cunha T.R., Baptista P., Silva P.A., 2017. Acquisition of bathymetric data from satellite images. Proceedings of the 8th SCACR – International Short Course/Conference on Applied Coastal Research, Santander, Spain, October 3-6

Adler-Golden S.M., Acharya P.K., Berk A., Matthew M.W., Gorodetzky D., 2005. Remote bathymetry of the littoral zone from AVIRIS, LASH, and QuickBird imagery. IEEE Trans. Geosci. Remote Sens. 43 (2), 337–347

Brusch S., Held P., Lehner S., Rosenthal W., Pleskachevsky A., 2011. Underwater bottom topography in coastal areas from TerraSAR-X data. Int. J. Remote Sens. 32 (16), 4527–4543

Capo S., Lubac B., Marieu V., Robinet A., Bru D., Bonneton P. (2014). Assessment of the decadal morphodynamic evolution of a mixed energy inlet using ocean color remote sensing. Ocean Dynamics, 64(10), 1517-1530

Chui C.K., 1992. An Introduction to Wavelets, 266p. Academic Press. (ISBN:0-12-174584-8)

Dekker A. G., Phinn S. R., Anstee J., Bissett P., Brando V. E., Casey B., Lynch M., 2011. Intercomparison of shallow water bathymetry, hydro-optics, and benthos mapping techniques in Australian and Caribbean coastal environments. Limnology and Oceanography: Methods, 9(9), 396-425

Fernández S., Lafon V., Regniers O., Debonnaire N., Stelzer K., Kalousi G., Constantin S., Gade M., Parcharidis I. Space for Shore -Deliverable 1.3 Product Validation Plan. Version 1. January 2020. 73 pp

Hedley J., Roelfsema C., Chollett I., Harborne A., Heron S., Weeks S., Ticzon V., 2016. Remote sensing of coral reefs for monitoring and management: a review. Remote Sensing, 8(2), 118

Lafon V., Dehouck A., Robinet A., Marieu V., Curti C., Durou N., 2014. Détection d'indicateurs géomorphologiques littoraux par télédétection à très haute résolution spatiale (pp. 601-610) - DOI:10.5150/jngcgc.2014.066

Lee Z., Carder K. L., Arnone, R. A., 2002. Deriving inherent optical properties from water color: a multiband quasi-analytical algorithm for optically deep waters. Applied optics, 41(27), 5755-5772

Lyzenga D.R., Malinas N.P., Tanis F.J., 2006. Multispectral bathymetry using a simple physically based algorithm. IEEE Trans Geosci. Remote Sens., 44(8):2251–2259

Mishra D., Narumalani S., Lawson M., Rundquist D., 2004. Bathymetric mapping using IKONOS multispectral data. GIScience & Remote Sensing, 41(4), 301-321

Mishra M.K., Ganguly D., Chauhan P., Ajai, 2014. Estimation of coastal bathymetry using RISAT-1 C-band microwave SAR data. IEEE Geosci. Remote Sens. Lett. 11 (3), 671–675

Pereira P., Baptista P., Cunha T., Silva P.A., Romão S., Lafon V., 2019. Estimation of the nearshore bathymetry from high temporal resolution Sentinel-1A C-band SAR data – A case study. Remote Sensing of Environment 223, 199-178

Stelzer K., Robinet A., Lafon V., Regniers O., Beguet B., Dehouck A., Baptista P., Fernández S., Kalousi G., Serban I., Echave I., Gade M., Bantouvaki K., Parcharidis I. Space for Shore -WP 1.2. Technical Specification Report. Version 1. July 2019. 77pp

Stumpf R. P., Holderied K., Sinclair M., 2003. Determination of water depth with high-resolution satellite imagery over variable bottom types. Limnology and Oceanography, 48(1part2), 547-556

Wiehle S., Pleskachevsky A., 2018. Bathymetry derived from Sentinel-1 Synthetic Aperture Radar data. In: 12th European Conference on Synthetic Aperture Radar Electronic Proceedings. Verband der Elektrotechnik Elektronik Informationstechnik e.V. Kartonhulle, Aachen, Germany, 978-3-8007-4636-1, pp. 1489

Zoffoli M., Frouin R., Kampel M., 2014. Water column correction for coral reef studies by remote sensing. Sensors, 14(9), 16881-16931

## 3.5 ALGORITHM GROUP 6 - EXTRACTION OF SUBMERGED MORPHOLOGICAL STRUCTURES AND CHANGES

### 3.5.1 Introduction

Coastal areas, especially beaches, are more and more threatened by the complex effects of climate change, which induces stresses such as increased storminess and overall, more frequent extreme events. These can lead to pressures that can take the form of increased erosion or modification of the maximum run-up limit. Since nearshore sandbars represent a natural defence system against these phenomena, monitoring the dynamics and behaviour of such morphological features can help coastal managers better prepare for coastal protection actions.

### 3.5.2 State-of-the-art

Various methods were widely used for the quantification of sandbar crest positions, ranging from seasonal and annual echo-sounder data to LiDAR surveys, X-band radar images, photographic and satellite imagery and video techniques (Roman-Rivera and Ellis, 2019).

However, applications of satellite imagery to date have been mainly restricted to nearshore satellite-derived bathymetry, which can be further used to derive the locations of sandbars. Nevertheless, there are situations when a good quality bathymetry is not possible to be obtained (such as areas with moderate to high turbidity), but it is still possible to extract the positions of the sandbars. Therefore, dedicated approaches are required. A recent study of Athanasiou *et al.,* 2018 discussed the suitability of using the Landsat 5, 7, 8 and Sentinel-2 satellite images for sandbar locations manual (visual) extraction in order to investigate decadal scale crescentic sandbar dynamics at Anmok beach in South Korea. To our knowledge, in exception to this work, there is no other study to date dealing with sandbar crest positions extraction (either manual or automatic) and analysis using high to moderate satellite images.

### 3.5.3 Algorithm 6a Submerged sand banks

#### 3.5.3.1 Algorithm Description

The algorithm is used to extract each submerged sandbar position using perpendicular profiles along the shoreline, based on multispectral satellite imagery (Tatui and Constantin, 2020). There are two distinct mechanisms (determined by the wave regime) that can be used to detect the position of a sandbar using a satellite image. The first one relies on a relative bathymetric estimation (not absolute values of water depth). This approach yields good results in case of low wave energy. In other situations, wave breaking occurs in the proximity of the shore, when the wave breaks on sandbars crest. It therefore creates a foam layer on the surface of the water, with very high reflectance response compared to the surrounding water. The maximum reflectance intensity of this foam region corresponds to the sandbar crest position (similar to video techniques). For these two scenarios, even if the observed object/phenomenon is different, it refers to the same morphometric features and the methodology relies on the same principle: reflectance spectrum is amplified over the areas where the sandbars are located.

- Input Data

The input data is represented by high to medium resolution multispectral satellite imagery. Visible and infrared (NIR or SWIR) wavelengths are required. The algorithm was tested on Sentine-2 data. Higher resolution images are expected to yield same quality results and even better.

- Algorithms

Several imagery pre-processing steps are required before the sandbar extraction can be performed, such as: scene cropping, resampling, masking areas that are not covered by water or combining the spectral bands from the visible domain, as to augment the increases in spectral response over the sandbar.

The procedure for sandbars extraction follows several steps, which are detailed hereafter:

1. A network of profiles, perpendicular to the shoreline is created.
2. Along each profile, the satellite combined reflectance values are extracted.
3. An exponential model is fitted to the graph of each profile perpendicular to the shoreline.
4. A normalisation of the profile is performed, by subtracting the model from the original data vector.
5. Using a moving window with a dimension, the maximum value within that region is computed. If the centre of the moving window corresponds with the identified maximum value, the position is qualified as a possible crest sandbar position. Also, if all the values within that moving window have a low standard deviation, then the point is not taken into consideration. Next, a supplementary filtration is performed, by removing points below the mean value of the positive numbers of the profile.
6. The final step is to compute a distance matrix between all points. Only those that have a neighbour closer than a specific distance are kept. Since the features that we hunt for are linear ones, occasional presence of just one point in space is considered not enough as to represent a sandbar.

- Tools

In order to implement the methodology, the following software and libraries were used: Geospatial Data Abstraction Library (GDAL) for satellite data pre-processing; R for the sandbar extraction.

- Outputs Products

Figure 3-33 below presents the sandbar position extracted from a Sentinel-2 image over different moments in time.

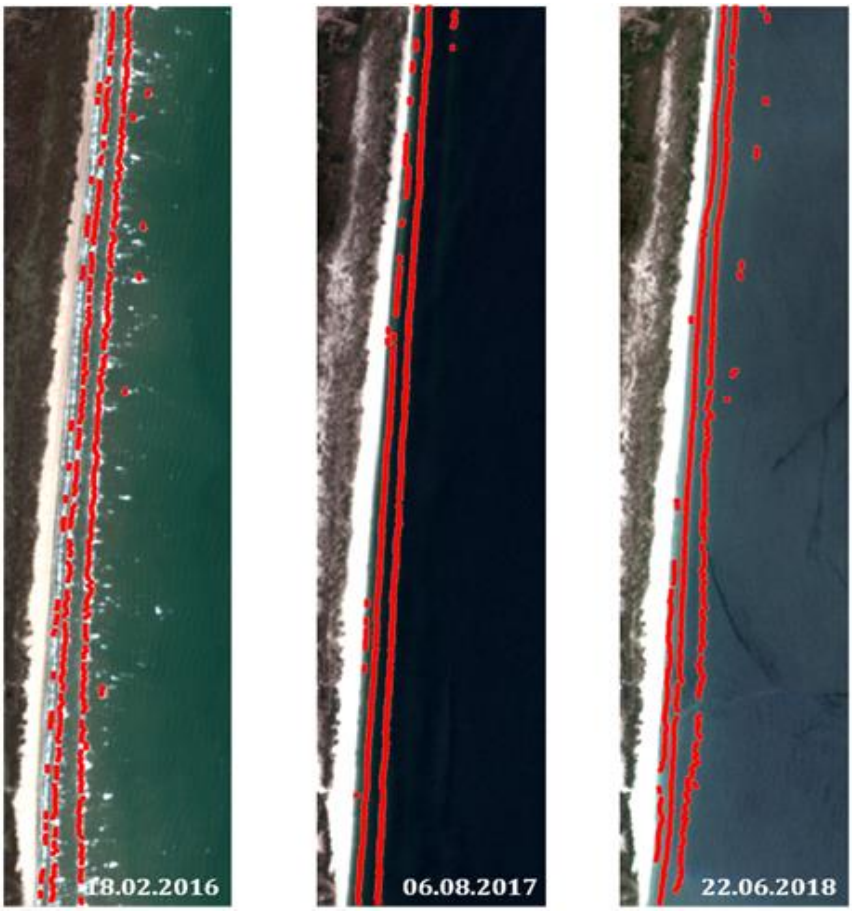


Figure 3-33 - *Sandbar position extracted from a Sentinel-2 image over different moments in time*

### 3.5.3.2 Validation

Validation activities consists of comparing the distance from shore (m) extracted from Sentinel-2 compared with distance from shore (m) determined from bathymetric measurements. The result of validation work performed for multiple match-up pairs are shown in the following Figure 3-34. Using the Sentinel-2 images the mean error (bias) in the cross-shore distance from the shoreline is of 6.2 m with a median error decreasing to 5.4 m and a mean relative error of approximately 6%. However, the use of higher-resolution images such as those acquired by Pléaides 1 may results in lower detection errors (higher accuracy).

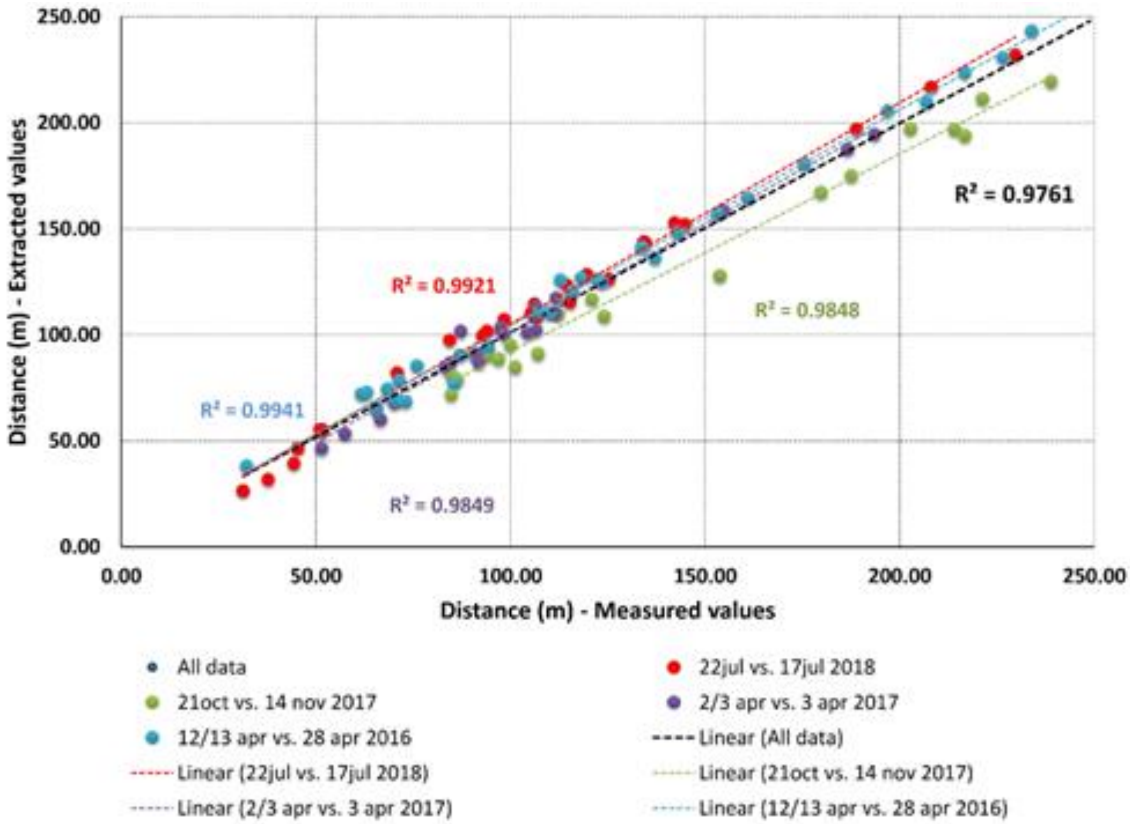


Figure 3-34 - *Match-up Analysis for distance of shore between DEM and derived sand banks*

### 3.5.3.3 Application Range and Maturity

The algorithm is developed using the new and innovative approach based on the combined reflectance of the submerged sand bars in the visible spectrum. The method has been applied on cloud free Sentinel-2 images from all seasons, covering various wave conditions, offered solid results. The area of interest is represented by the coastal area of Danube Delta, between Sfantu Gheorghe and Sulina.

The algorithm was tested on more than 3 years of satellite data and was validated using consistent *in situ* measurements. The maturity of implementation allows replication in other areas and using other satellite data types.

## 3.5.4 Algorithm 6b - Mapping change of submerged sandbars/sand ridges

### 3.5.4.1 Algorithm Description

This algorithm to identify submerged sandbars or ridges in remote sensing images is based on the spatial analysis of the spectral reflectance values in an optical band. A submerged sandbar or ridge can are characterised by as local maxima in the reflectance value field. A well-known ridge detector has been developed using the Hessian matrix (Mikolajczyk *et al.,* 2005).

- Input Data

The algorithm has been developed and tested on Sentinel-2 data. The Sentinel-2 band 3 at 10m spatial resolution seems particularly well suited because the sandbars are visible and the noise is acceptable.

- Algorithms

A few pre-processing steps are required before the sandbar ridge detection algorithm can be applied such as: QA of the inputs regarding the tides, turbidity of the water, sun glint effects, pixel identification including cloud screening and land/water discrimination as well as noise filtering.

The following steps have been performed:

- Calculation of the second order derivative matrix also called the "Hessian matrix using the Scharr operator (Scharr, 2000) and the Canny algorithm (Canny, 1986)

$$\begin{pmatrix} H_{xx} & H_{xy} \\ H_{xy} & H_{yy} \end{pmatrix} = \begin{pmatrix} \frac{\partial^2 g}{\partial x^2} & \frac{\partial^2 g}{\partial x\,\partial y} \\ \frac{\partial^2 g}{\partial x\,\partial y} & \frac{\partial^2 g}{\partial x^2} \end{pmatrix}$$

with g(x,y) is the spectral reflectance, and x, y are the image coordinates (not the geographic coordinates)

- Calculation of the major eigenvalue

$$major\ eigenvalue = \frac{1}{2}\left(H_{xx} + H_{yy} + \sqrt{H_{xx}^2 + 4H_{xy}^2 - 2H_{xx}H_{yy} + H_{yy}^2}\right)$$

- Thresholding and linking procedure

- Tools:

The processor is implemented as a plugin for the ESA SNAP software

- Outputs Products

The output product includes several bands including the original image and the retrieved sandbars/ridges. The following Figure 3-35 presents the original image and the over-laid detected sandbars.

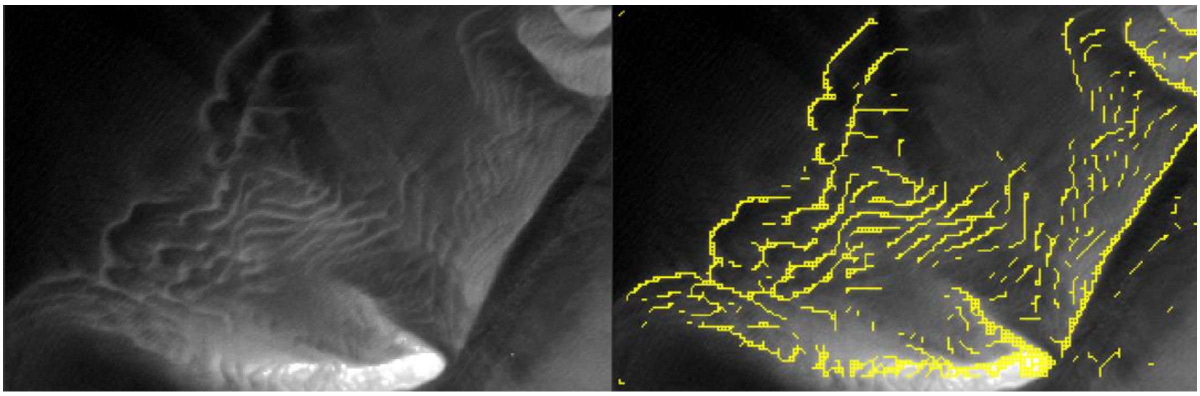

Figure 3-35 - *Subset of the Sentinel-2 band 3 image of 2016-05-09 (left) and the over-laid detected sandbars in yellow (right)*

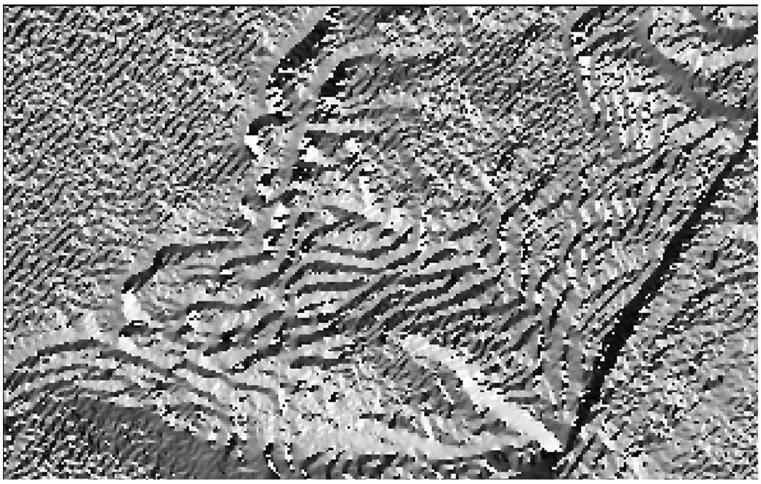

Figure 3-36 - *Gradient direction of band 3 as processing step for identification of the sandbar ridges.*

#### 3.5.4.2 Validation

The validation activities will comprise the processing of a set of Sentinel 2 images and the visual analysis.

#### 3.5.4.3 Application Range and Maturity

The assessment of the application range is under investigation.

### 3.5.5 References

Athanasiou P., de Boer W., Yoo J., Ranasinghe R., Reniers A., 2018. Analysing decadal-scale crescentic bar dynamics using satellite imagery: A case study at Anmok beach, South Korea. Mar. Geol. 405 https://doi.org/10.1016/j.margeo.2018.07.013

Canny J., A Computational Approach to Edge Detection. IEEE Transactions on Pattern Analysis and Machine Intelligence, Vol. PAMI-8, No. 6, November 1986

Mikolajczyk K., Tuytelaars T., Schmid C., Zisserman A., Matas J., Schaffalitzky F., Kadir T., Van Gool L. A comparison of affine region detectors. International Journal of Computer Vision 65(1/2):43-72, 2005, DOI: 10.1007/s11263-005-3848-x

Roman-Rivera M.A., Ellis J.T., 2019. A synthetic review of remote sensing applications to detect nearshore bars. Marine Geology, 408, p. 144-153

Scharr H., Optimale Operatoren in der Digitalen Bildverarbeitung. Dissertation: Ruprecht-Karls-Universität Heidelberg, 2000

Tatui F., Constantin S., 2020. Nearshore sandbar crest position dynamics analysed based on Earth Observation data. Remote Sens. Environ. 237. doi:10.1016/j.rse.2019.111555

# 4. CONCLUSION AND OUTLOOK

This document provides an overview of all algorithms available for producing indicators and finally the services to the users. The mapping of the algorithms to the user requirements provide a good assessment on which algorithms will be used for which coastal type and which site. It also gives the overall picture of the possible combinations of algorithm and EO data type (HR vs VHR) that can be used to address coastal erosion on the short-term (event to annual timescales) with a maximal accuracy or on the long term (interannual to decadal scales) usually coming with a poorer accuracy.

The algorithms differ in their level of maturity and while some are already mature, well validated and applied to many different locations, others are on an experimental stage. This document will be updated accordingly, providing further input for validation and application range of the single algorithms. This should allow us to identify which algorithm performs best for each couple indicator / site, if not already done. These conclusions could then be extended at a larger scale to other coastal European regions.

# 5. ANNEX

An overview table of the not used algorithms from the first phase who are fully described in Technical Specification 1.1 from last year:

| Algorithm Group | Algorithm | Maturity level | Partner | Suitable for: Product Name |
|---|---|---|---|---|
| **Water Line and Creek Edge Detection** | **Algorithm 2b** Water line detection using NDWI **(this algorithm has been regrouped in 2a for phase 2) | 3 | I-Sea | Waterline (sea/land interface)<br>Middle of swash zone<br>Maximum swash (or run-up) excursion during major storms<br>Beach width |
| | **Algorithm 2c** Water line detection using a supervised classification process | 2 | I-Sea | Waterline (sea/land interface)<br>Middle of swash zone<br>Maximum swash (or run-up) excursion during major storms<br>Beach width |
| | **Algorithm 2d** Water line detection using binary products from SAR amplitude data | 1 | Harokopio University | Waterline (sea/land interface)<br>Middle of swash zone<br>Maximum swash (or run-up) excursion during major storms<br>Beach width |
| **Extraction of subaerial morphological structures and changes** | **Algorithm 3a** Dune foot extraction using the cross-shore variation of first-order texture metrics from VHR optical data | 2 | I-Sea | Dune foot<br>Middle of swash zone<br>Maximum swash (or run-up) excursion during major storms |
| | **Algorithm 3b** Dune foot extraction based on beach/dune slope from DEM | 1 | I-Sea | Dune foot |
| | **Algorithm 3c** | 1 | I-Sea | Cliff foot |

| | | | | |
|---|---|---|---|---|
| | Cliff line extraction using the cross-shore variation of the beach/cliff slope from DEM | | | Cliff apex |
| | **Algorithm 3g**<br>Intertidal creek morphological characteristics | 1 | Brockmann Consult | Tidal creeks: number, length, form, form and number of tidal creek endings<br>Erosion at tidal creek edges |
| **Bathymetry** | **Algorithm 4a**<br>Empirical model to retrieve bathymetry from HR/VHR optical data | 3 | I-Sea | Bathymetry |
| **Classification methods** | **Algorithm 5a**<br>Supervised classification approaches based on optical data | 3 | I-Sea | Underwater seabed type (sandy/rocky/vegetated)<br>Waterline (sea/land interface)<br>Maximum swash (or run-up) excursion during major storms<br>Coastal and intertidal habitat and land cover mapping |
| | **Algorithm 5b**<br>Classification based on texture information derived from SAR amplitude data | 3 | Harris | Coastal and intertidal habitat and land cover mapping |